Fatigue response of wire-arc additive manufactured nickel-aluminum bronze (NAB) in the post-annealed condition

International Journal of Fatigue 187 (2024) 108472

Contents lists available at ScienceDirect

International Journal of Fatigue

journal homepage: www.elsevier.com/locate/ijfatigue

Fatigue response of wire-arc additive manufactured nickel-aluminum bronze (NAB) in the post-annealed condition

Shawkat I. Shakil [a], Sajad Shakerin [b], Keivan Rahmdel [c,d], Mohsen Mohammadi [b], Andrea Tridello [e], Davide S. Paolino [e], Shuai Shao [c,d], Nima Shamsaei [c,d], Meysam Haghshenas [a,*]

[a] Fatigue, Fracture, and Failure Laboratory (F3L), Department of Mechanical, Industrial, and Manufacturing Engineering (MIME), The University of Toledo, OH, USA
[b] Marine Additive Manufacturing Centre of Excellence (MAMCE), University of New Brunswick, Fredericton, NB E3B 5A1, Canada
[c] National Center for Additive Manufacturing Excellence (NCAME), Auburn University, Auburn, AL 36849, USA
[d] Department of Mechanical Engineering, Auburn University, Auburn, AL 36849, USA
[e] Dipartimento di Ingegneria Meccanica e Aerospaziale, Politecnico di Torino, Corso Duca Degli Abruzzi 24, 10129 Torino, Italy

ARTICLE INFO

Keywords:
Wire arc additive manufacturing
WAAM
Nickel aluminum-bronze
NAB
Fatigue

ABSTRACT

Nickel-aluminum bronze (NAB) is chosen for critical applications like marine propellers, pump components, and offshore structures due to its exceptional mechanical properties and corrosion resistance. Considering the utmost importance of the fatigue performance of NAB in such applications, this study investigates the fatigue performance of wire arc additive manufactured (WAAM) NAB in the annealed (675 °C for 6 h then furnace cooling) condition. To this end, static mechanical properties were evaluated using uniaxial tensile testing, while fatigue properties were assessed through fully reversed tests conducted at ambient temperature. Electron backscatter diffraction (EBSD) was utilized for the examination of the texture, and grain size distribution in annealed WAAM NAB. Additionally, scanning electron microscopy was employed to inspect fatigue-fractured specimens, while the analysis of EBSD was conducted to examine the deformation behavior beneath the crack initiation zone. The results provide insights into the fatigue life, crack initiation, and propagation characteristics of WAAM NAB relative to the cast counter material. The findings of this research provide valuable insights into the mechanical properties, microstructural characteristics, and fatigue response of WAAM NAB, informing the design of fatigue-resistant components and supporting the reliable utilization of WAAM NAB in demanding applications such as the marine and naval industries.

1. Introduction

Wire arc additive manufacturing (WAAM) has emerged as an efficient and reliable technique for fabricating large-size metallic structures with complicated geometry, allowing significant advantages in terms of cost, time, and design flexibility [1,2]. In contemporary applications, WAAM has been utilized to produce Nickel-Aluminum Bronze (NAB), a copper-based alloy distinguished by the inclusion of Al, Fe, and Ni as major alloying elements. NAB finds significance in the marine sector, particularly in the construction of essential components such as ship propellers, pumps, and valves, among other maritime applications [3]. For such applications, excellent mechanical properties, a desirable combination of strength, ductility and toughness, and corrosion resistance are required [4–6]. To this end, understanding the fatigue behavior of WAAM NAB components is crucial for assessing their reliability/integrity and ensuring their successful integration in demanding applications.

NAB is a microstructurally complex alloy and contains copper-rich α-phase, martensitic β' phase (or retained β), and various intermetallic phases (referred to as κ phase) [7,8]. The marked disparity in cooling rates between WAAM and conventional casting techniques leads to the refinement of microstructural features in NAB produced through WAAM. Depending on the location, distribution, morphology, composition, and order of formation, the κ phases are denoted as κ_I, κ_{II}, κ_{III}, and κ_{IV} [7,9]. Due to the high cooling rates, i.e., ~10 – 1000 °C/s (based on the variation of WAAM process parameters) [10,11], the κ_I precipitate does not form [12]. According to Dharmendra et al. [13], heat treatment gives rise to another κ phase (Ni-rich, needle-like morphology) denoted as κ_V.

* Corresponding author.
E-mail address: meysam.haghshenas@utoledo.edu (M. Haghshenas).

https://doi.org/10.1016/j.ijfatigue.2024.108472
Received 12 April 2024; Received in revised form 10 June 2024; Accepted 19 June 2024
Available online 20 June 2024

Nomenclature

Abbreviations

ASTM	American Society for Testing Materials
β	Scale Parameter
CDF	Cumulative Distribution Function
CRSS	Critical Resolved Shear Stress
D_e	Equivalent Diameter
DCEP	Direct Current Electrode Positive
EBSD	Electron Backscatter Diffraction
EDM	Electrical Discharge Machining
EDS	Energy Dispersive Spectroscopy
FEA	Finite Element Analysis
FSP	Friction Stir Processed
HV	Vickers Hardness
HCF	High Cycle Fatigue
HT	Heat Treated
IAMA	Internal Average Misorientation Angles
IPF	Inverse Pole Figure
κ	Intermetallic Phase (κ_I, κ_{II}, κ_{III}, κ_{IV}, κ_V)
KAM	Kernel Average Misorientation
LCF	Low Cycle Fatigue
LEVD	Largest Extreme Value Distribution
MRD	Multiple Random Distributions
NAB	Nickel-Aluminum Bronze
N_f	Number of Cycles
RVE	Representative Volume Element
S-N	Stress – Number of cycles to failure
SNP	S-N-Probability of Failure
SSDs	Statistically Stored Dislocations
UTS	Ultimate Tensile Strength
WAAM	Wire Arc Additive Manufacturing
WRA	White Rough Area
XCT or μ-CT	X-ray Computed micro-Tomography
μ	Location Parameter
YS	Yield Stress

Some literature [14–18] exists on NAB regarding its microstructure, fatigue behavior, and corrosion fatigue behavior, although most of which has been for the cast form of the alloy. Considering the in-service failure of NAB components in the high cycle fatigue (HCF) domain, Chakrabarti et al. [14] investigated the effect of mean stress variation and size and location of defects on the HCF behavior of cast NAB. Expectedly, fatigue life decreased significantly with the increase in mean stress and size of defects. They reported that fatigue failure due to a larger defect located deep within the sample corresponded to a longer life than that due to a smaller defect positioned near the surface. Xu et al. [18] investigated the influence of secondary phases on the fatigue crack growth behavior of as-cast, annealed (675 °C for 2 h), and normalized (920 °C for 1 h) NAB. The as-cast NAB with α, β′, κ_{II}, κ_{III}, and κ_{IV} phases had the highest fatigue crack growth rate. In contrast, annealed NAB, enriched in κ_{III}, demonstrated a moderate rate. The normalized NAB, rich in β′ and κ_{IV} fine precipitates but lacking κ_{II} and κ_{III} phases, showed the slowest rate of fatigue crack growth. In other studies, Gao et al. [19] investigated the effect of laser shock peening on residual stress and surface roughness and their relation with the fatigue of cast NAB. Ding et al. [20] studied the differences between the fatigue life of NAB specimens in air and a corrosive medium (3.5 % NaCl solution) and found that in the case of corrosion fatigue, acidification and dealumination, which decreases fatigue threshold and increases the crack growth rate, occur. In another study, Mshana et al. [21] studied the four-point rotating bending fatigue response (in the high cycle regime) of cast NAB in air and a 3.0 % NaCl solution and reported that an anti-corrosion heat treatment (700 °C for 6 h followed by air cooling) improved the fatigue strength considerably. Though the precipitation hardening effect of heat treatment improved the fatigue strength there was an insignificant difference in the fatigue crack growth rate of the specimens in both media. Lv et al. [22] investigated the fatigue crack growth mechanism of friction stir processed (FSP) NAB, identifying that microstructural modifications, such as refinement of grains and intermetallics, nano-twining, and strain hardening play a crucial role in inhibiting fatigue crack growth.

There has been a lack of fatigue studies specifically focused on NAB produced through WAAM. This gap of knowledge highlights a novel and underexplored area of research, holding the promise of providing distinctive insights that could contribute to the enhancement of fatigue properties in WAAM NAB components. It is worth noting that microstructure [12,23,24], tensile [12,13,25], and nano/micro-mechanical [26,27] properties of WAAM NAB have been studied extensively in as-built and heat-treated (e.g., annealed) conditions. The volumetric defects arising from WAAM, such as porosity, delamination, lack of fusion, and oxide-based inclusions, coupled with the heat input during the WAAM deposition process and subsequent thermal cycling, may directly influence the fatigue response of the fabricated material. Therefore, the fatigue response of WAAM NAB is expected to be different than cast NAB.

Since fatigue is a prevalent factor contributing to the failure of in-service NAB components, a comprehensive examination of the fatigue response of WAAM NAB is deemed crucial before its integration into real-world applications. Considering the NAB-built components experience a range of cyclic loads in their respective applications, it is imperative to conduct a comprehensive assessment encompassing both low cycle fatigue (LCF) and HCF considerations. Specifically, on HCF characteristics of WAAM NAB under fully reversed conditions, Bercelli et al [28] conducted a probabilistic approach considering the process-induced volumetric defects (i.e., gas porosities). Their stress-life (S-N) data displayed substantial scatter due to the presence of large, isolated pores, indicating that the samples do not represent a representative volume element (RVE) for fatigue behavior. Despite this scatter, the machined WAAM material demonstrated superior overall fatigue performance compared to the as-cast NAB material. Bercelli et al. [28] also established a numerical methodology based on their probabilistic fatigue model and showed that the interpolated S-N-probability of failure (SNP) curves from a finite element analysis (FEA) pore database align well with experimental results. In another study by Bercelli et al. [29], the effects of process-induced surface roughness on the fatigue performance of as-built WAAM NAB was experimentally studied at a loading ratio of 0.1. They showed that the crack initiation sites are somewhat correlated with highly stressed regions on the rough surface. Additionally, they introduced an image post-processing technique to monitor crack propagation. Their proposed image post-processing techniques on infrared data enable the tracking of fatigue crack propagation of multiple cracks over a large area. This allows for the characterization of propagation kinetics, such as those described by the Paris Law.

Considering the presented literature review, the objective of this study is to systematically quantify the force-controlled fatigue response of WAAM NAB at room temperature under laboratory air conditions in its post-annealed state (675 °C for 6 h followed by furnace cooling). Conducting a fatigue analysis of this multiphase NAB alloy in an ambient air environment is a significant step toward explaining the influence of WAAM-induced microstructure and volumetric defects (e.g., inclusions, gas porosities, lack of fusion) on fatigue crack behavior while mitigating the confounding effects of environmental factors such as corrosion. The generated S–N data and the assessment of the controlling mechanisms of ambient-air fatigue failure in WAAM NAB serve as a baseline for

Table 1
Chemical composition of studied material (WAAM NAB).

Elements	Cu	Al	Ni	Fe	Mn	Si	Zn	P	Co, Sn, Pb, Ag
Weight %	Balance	8.78	5.16	3.29	0.92	0.04	0.02	<0.005	<0.001

Table 2
WAAM process parameters employed for printing (WAAM) NAB wall.

Wire Size	1.14 mm
Polarity/Transfer Mode	DCEP/Pulse Spray
Bead width	12.02 mm
Number of beads per layer	5
Infill bead Heat Input	5.04–6.02 kJ/cm
Maximum Interlayer Temperature	200 °C
Interpass Temperature	200 °C

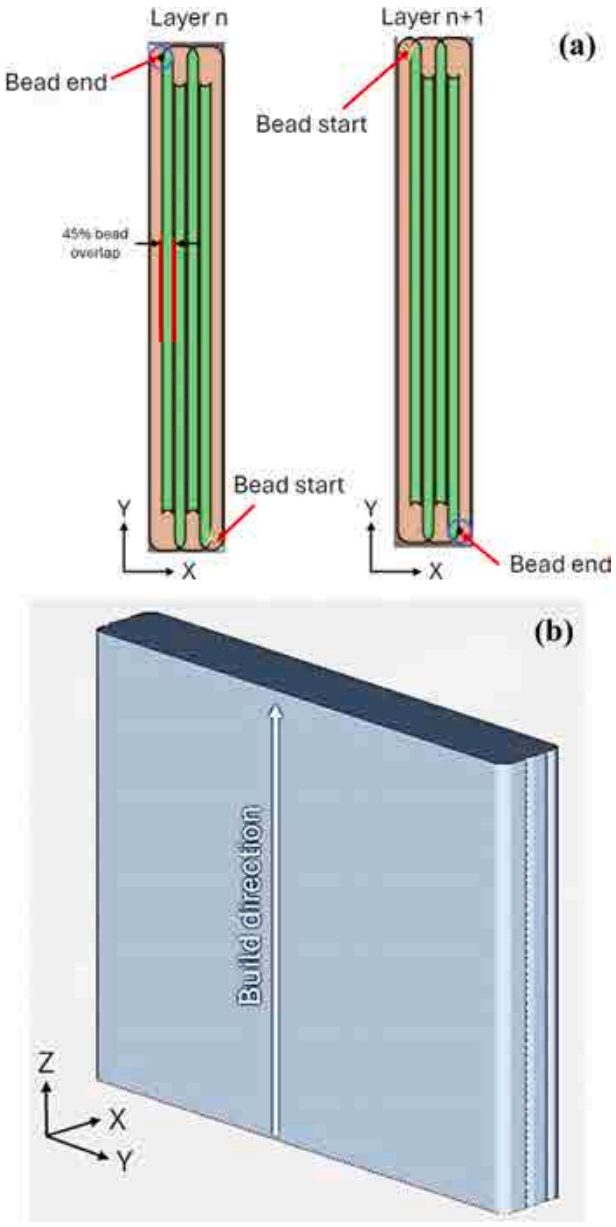

Fig. 1. (a) Printing scheme illustrating the walls' start and end points, the employed overlap, and (b) the wall model in the slicing software.

quantifying the in-situ and ex-situ corrosion fatigue characteristics of WAAM NAB. This alloy is primarily used in various parts and components in marine and naval applications, where it is exposed to corrosive environments and cyclic loading; therefore, the characterization of corrosion fatigue in WAAM NAB, compared to cast counterparts, is of main importance. Advanced microscopy techniques are employed in this study to establish and analyze correlations between processing parameters, resultant microstructure, WAAM-induced volumetric defects, and fatigue behavior. This approach aims to provide a deeper understanding of the underlying mechanisms driving the fatigue performance of WAAM NAB, contributing to the broader body of knowledge on the structural integrity and reliability of copper-based AM materials (e.g., NAB) relative to conventionally fabricated (e.g., cast) counter materials.

2. Experimental procedure

The material investigated in this study is a NAB alloy fabricated by WAAM. For this study, the printed walls were supplied by Lincoln Electric®, and the chemical composition of the material is given in Table 1. The WAAM print parameters were developed by Lincoln Electric® and listed in Table 2. The employed WAAM process for NAB involves printing each layer to a width equivalent to five bead thicknesses using a continuous serpentine path. The starting locations of the beads alternate with each successive layer to enhance structural integrity. A 45 % overlap between bead paths is maintained to ensure adequate bonding and minimize porosity. The height of each layer is approximately 1.8 mm, contributing to the precision and quality of the AM process. Fig. 1a shows the printing scheme of the walls' start and end points and the employed overlap as well as the wall model in the slicing software (Fig. 1b).

To investigate the influence of heat treatment on WAAM NAB components, the printed NAB wall underwent testing and characterization in an annealed condition. The annealing process was executed at 675 °C for 6 h, followed by a controlled furnace cooling protocol. For preparing the tensile and fatigue specimens, the NAB wall was first cut from the base plate using wire electrical discharge machining (EDM) and then 3 tensile and 21 fatigue test specimens were machined out following ASTM standards E08 [30] and E466 [31], respectively.

Fig. 2 illustrates several aspects of the experimental setup including the specific locations where the tensile and fatigue specimens were extracted from the printed wall (Fig. 2a), detailed top and front views of the walls to provide a comprehensive understanding of their structure (Fig. 2b), and the final machined tensile and fatigue specimens prepared for testing (Fig. 2c). Fatigue testing was conducted using an Instron 8822 servo-hydraulic test machine with a load capacity of 100 kN. The tests were carried out under fully reversed conditions ($R = -1$) at room temperature, with a fixed frequency of 10 Hz. After testing, the fractured specimens were carefully analyzed using fractography techniques to assess the mode of fatigue crack initiation and propagation. The fractography analysis involved scanning electron microscopy (SEM) using an FEI Quanta 3D FEG system combined with energy dispersive spectroscopy (EDS).

To examine the defect characteristics, X-ray computed tomography (XCT) scans were performed on annealed NAB specimens using a Zeiss Xradia 620 Versa system. The location and size of volumetric defects inside the manufactured specimens were extracted from the gauge section of fatigue coupons via the scans. The distance of the X-ray source and detector from the coupon was adjusted to achieve a 5.5 μm voxel size, aiming for maximum pixel resolution while scanning the entire diameter of the gage section. The X-ray source operated at a voltage of

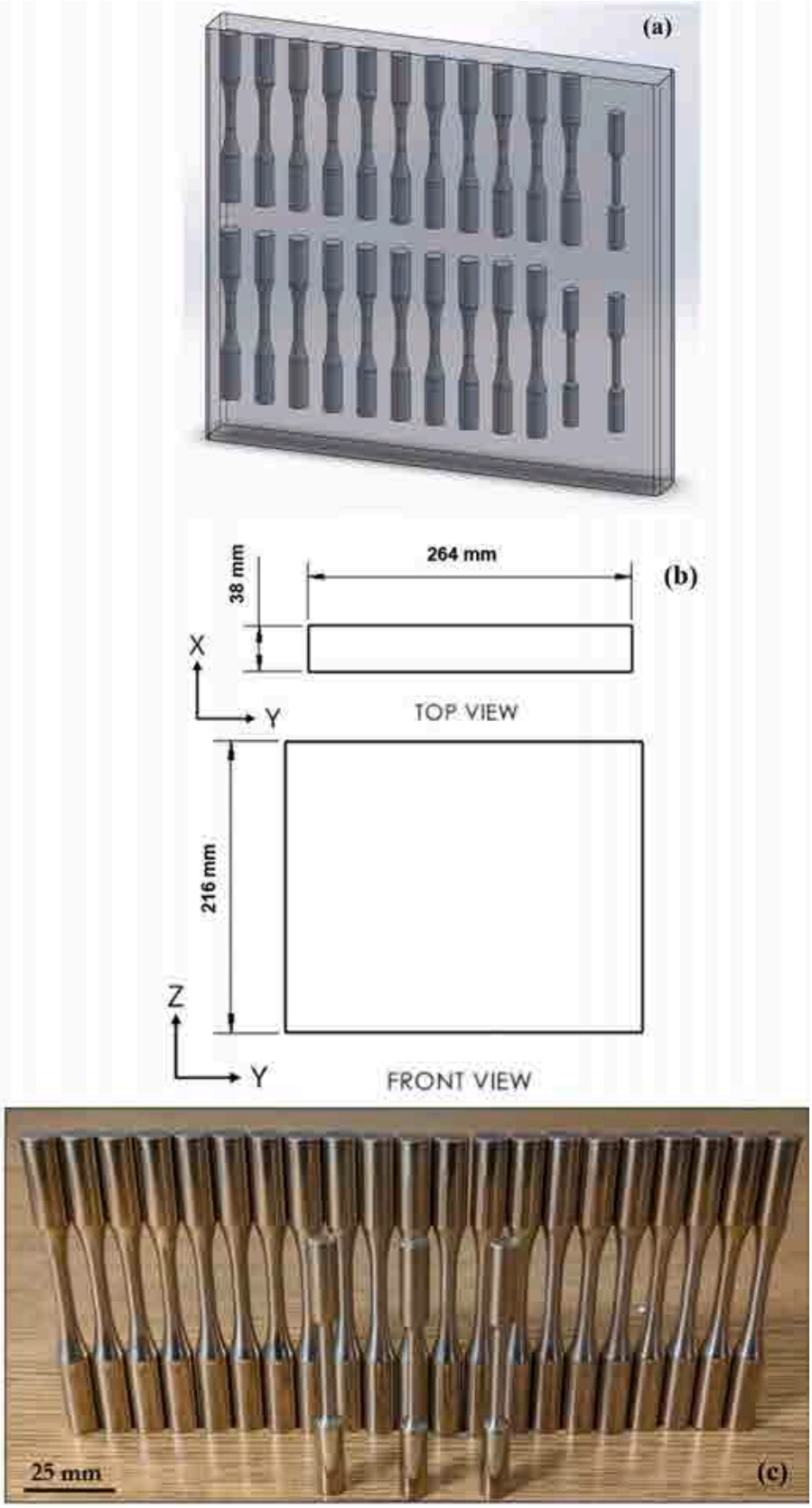

Fig. 2. (a) location of tensile and fatigue specimens in the printed wall, (b) top and front views of the walls, (c) machined tensile and fatigue specimens.

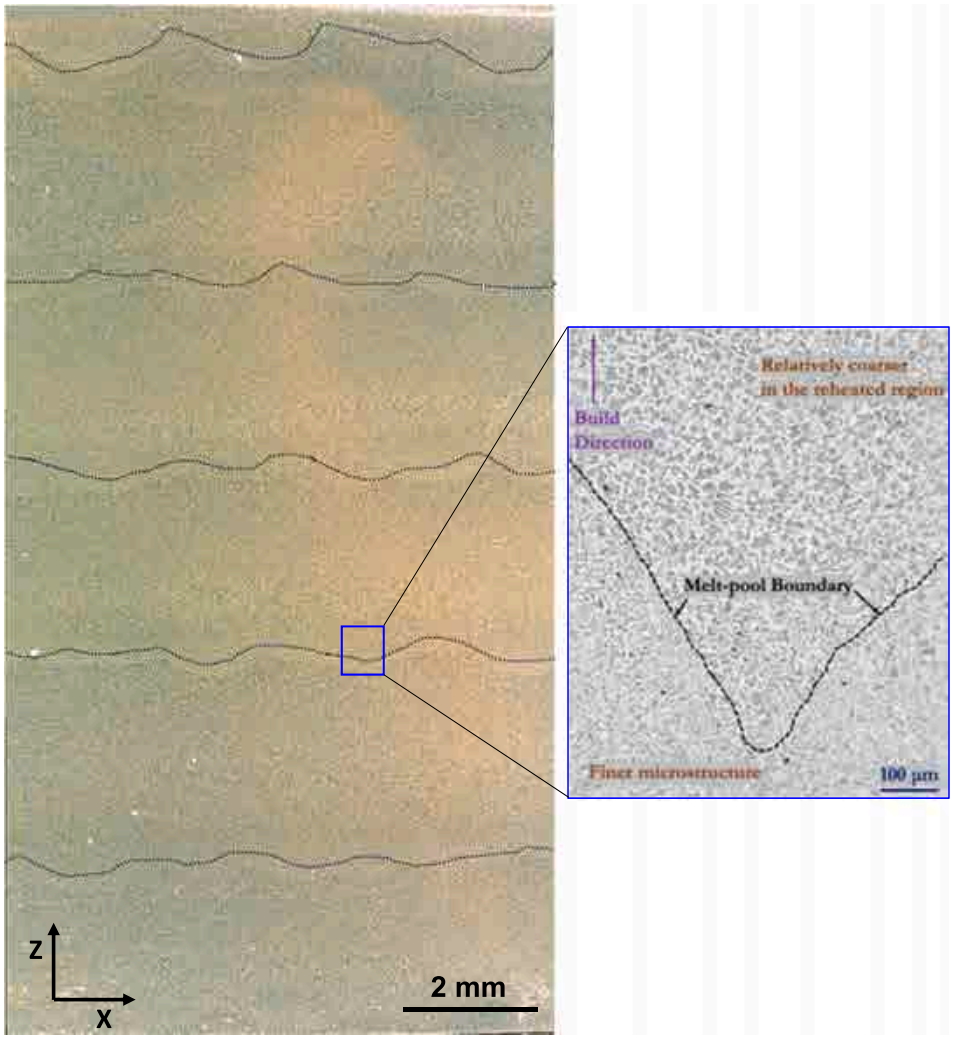

Fig. 3. Macrograph of the starting material (X-Z plane) which shows a banded structure of the deposited wall. The layer bands are representative of deposition passes. The blue box shows the zoomed-in micrograph of the coarse and fine-grain structures above and below the melt pool boundary. (For interpretation of the references to color in this figure legend, the reader is referred to the web version of this article.)

150 kV and a current of 153.4 μA, and an "HE6″ filter was used to condition the X-ray for higher transmittance. Furthermore, a 2.3 s exposure time was chosen with these settings to achieve optimal photon intensity. Zeiss software was used to reconstruct raw XCT files, followed by image analysis using ImageJ and Dragonfly software.

Optical microscopy and SEM-based electron backscatter diffraction (EBSD) analysis were carried out on the starting microstructure of annealed samples as well as on the samples extracted from the fatigue fractured specimens focusing on the crack initiation zone. The fatigue-damaged specimens were precisely cut in the direction of the applied load (i.e., the sectioned plane was parallel to the build direction), close to the crack initiation site, utilizing an electro-discharge machining (EDM) technique. The EBSD patterns were captured with a Scios 2 DualBeam electron microscope equipped with a Symmetry S Oxford Instrument detector. The EBSD parameters included a specimen tilt angle of 70°, an electron voltage of 20 kV, a step size of 200 nm, and a resolution of 1,024,768 × pixels. Subsequently, the EBSD data was subjected to post-processing using TSL OIM Analysis 8 and HKL Channel 5 software. The texture analysis was presented in inverse pole figure (IPF) maps and pole figures, while the strain analysis was performed based on kernel average misorientation (KAM) and results are presented in the form of deformation maps through partitioning the deformed, substructured, and recrystallized grains.

3. Results and discussion

The results obtained in terms of microstructural observation, porosity analysis, and tensile and fatigue characteristics (including fractography) are divided into the following subsections and discussed accordingly.

3.1. Starting microstructure

Fig. 3 shows the optical macrograph of the material structure exhibiting regular layer band patterns of heterogeneities that align with the various build layers of the WAAM process (e.g., distinct weld beads that form patterns spanning several millimeters). The zoomed-in micrograph in Fig. 3 shows coarse and fine-grained structures, with α-dendrites (bright contrast) and inter-dendritic regions (dark contrast) around (i.e., below and above) the melt pool boundaries. Due to the layer-by-layer deposition process inherent in the WAAM process, the upper region of the previously deposited layer is subjected to reheating. This reheating occurs as subsequent layers are deposited, causing the material in the upper region to experience thermal cycles. As a result, the microstructure in this reheated zone becomes coarser (grain growth) compared to the underlying material that does not undergo the same extent of thermal exposure.

EBSD analysis was systematically conducted to unravel the

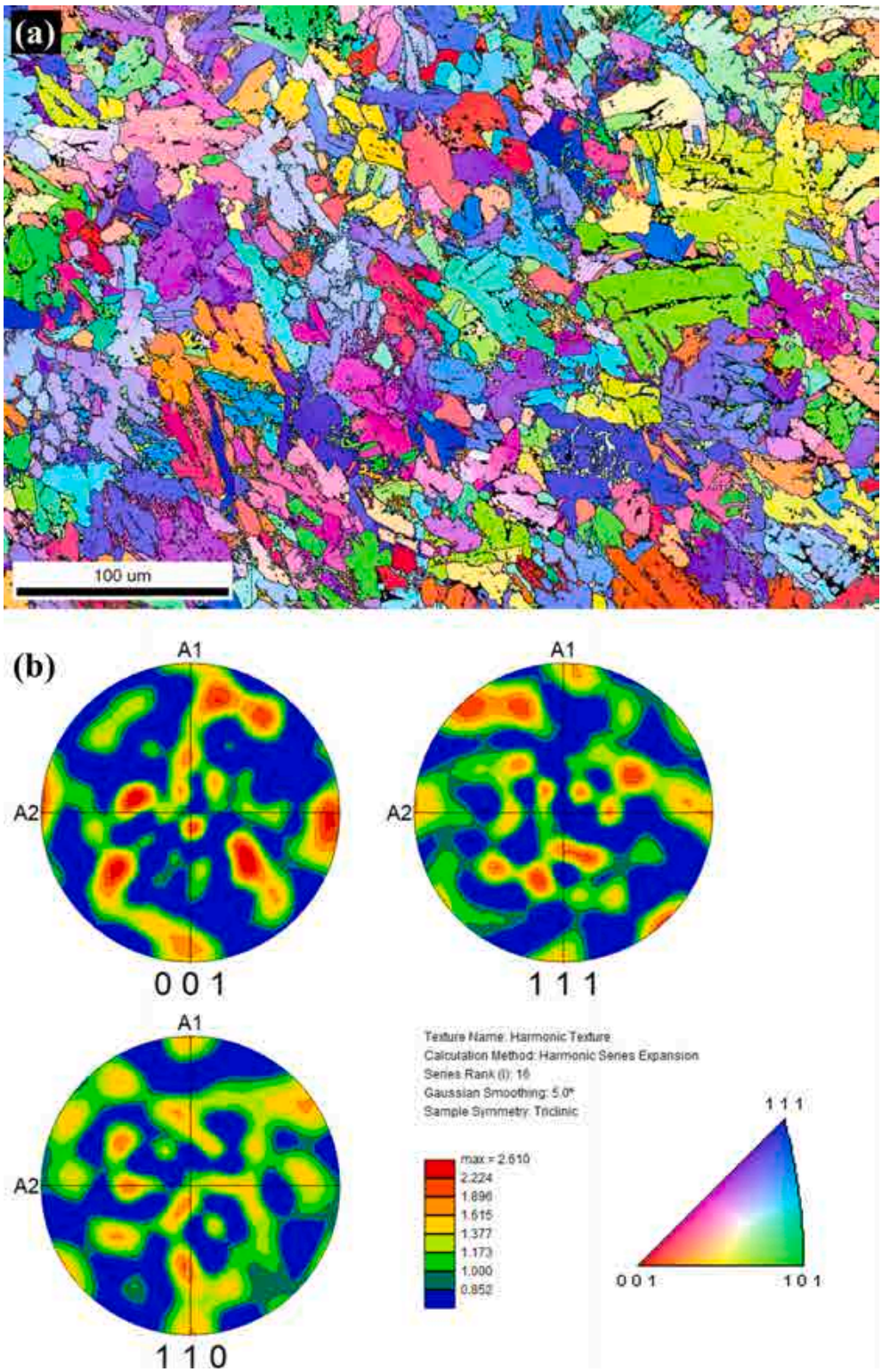

Fig. 4. (a) EBSD IPF map and (b) pole figures of annealed WAAM NAB.

intricacies of microstructure, texture, and grain size distribution within the annealed WAAM NAB. In Fig. 4a, the EBSD IPF map illustrates the refined grain size, a consequence of the rapid cooling and solidification inherent in the WAAM process. Notably, the average grain diameter was quantified at 2.46 ± 3.70 μm, underscoring the fine-grained nature of the material compared to traditional cast counterparts (grain size ~ 40 μm) [32]. To visualize the texture the pole figure is presented in Fig. 4b. Remarkably, the patterns of the pole figures and the multiple random distributions (MRD) value of 2.61 in Fig. 4b signify a rather random texture in the annealed condition. This randomness, indicative of a balanced crystallographic orientation distribution, may contribute to the isotropic behavior of the material. This balanced crystallographic orientation distribution contributes to the material's structural stability because there are no preferred paths for crack propagation. Therefore, understanding the absence of texture in a material helps assess its stability and predict its behavior under various conditions. Furthermore,

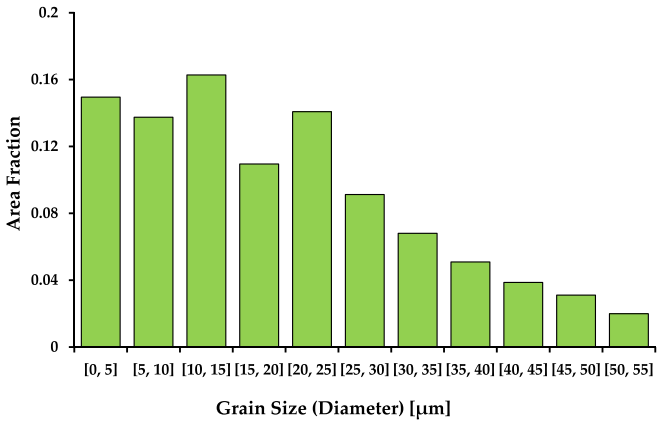

Fig. 5. Grain size distribution of annealed WAAM NAB.

the corresponding grain size distribution displayed in Fig. 5 provides a comprehensive overview of the annealed sample's microstructure. Texture and grain size in a material reveal a complex connection between processing conditions and the properties it ends up having.

The fatigue crack behavior of NAB is notably influenced by its microstructural features. That is, the configuration and fraction of intermetallic phases emerge as key determinants affecting the characteristics of fatigue crack propagation. Besides, processing routes (e.g., casting versus additive manufacturing) and post-fabrication heat treatment significantly alter the morphology, distribution, and volume fraction of these phases and therefore the fatigue crack behavior [13,33].

This refined microstructure (i.e., grain size of 2.46 ± 3.70 μm for WAAM vs ~40 μm for cast [32]) is anticipated to play a crucial role in NAB's fatigue behavior. Indeed, the smaller grain size and finer precipitates contribute to increased static mechanical properties. Based on the previous studies by the authors [13,34], when comparing as-WAAM with WAAM'd and post-annealed (675 °C for 6 h) states, several

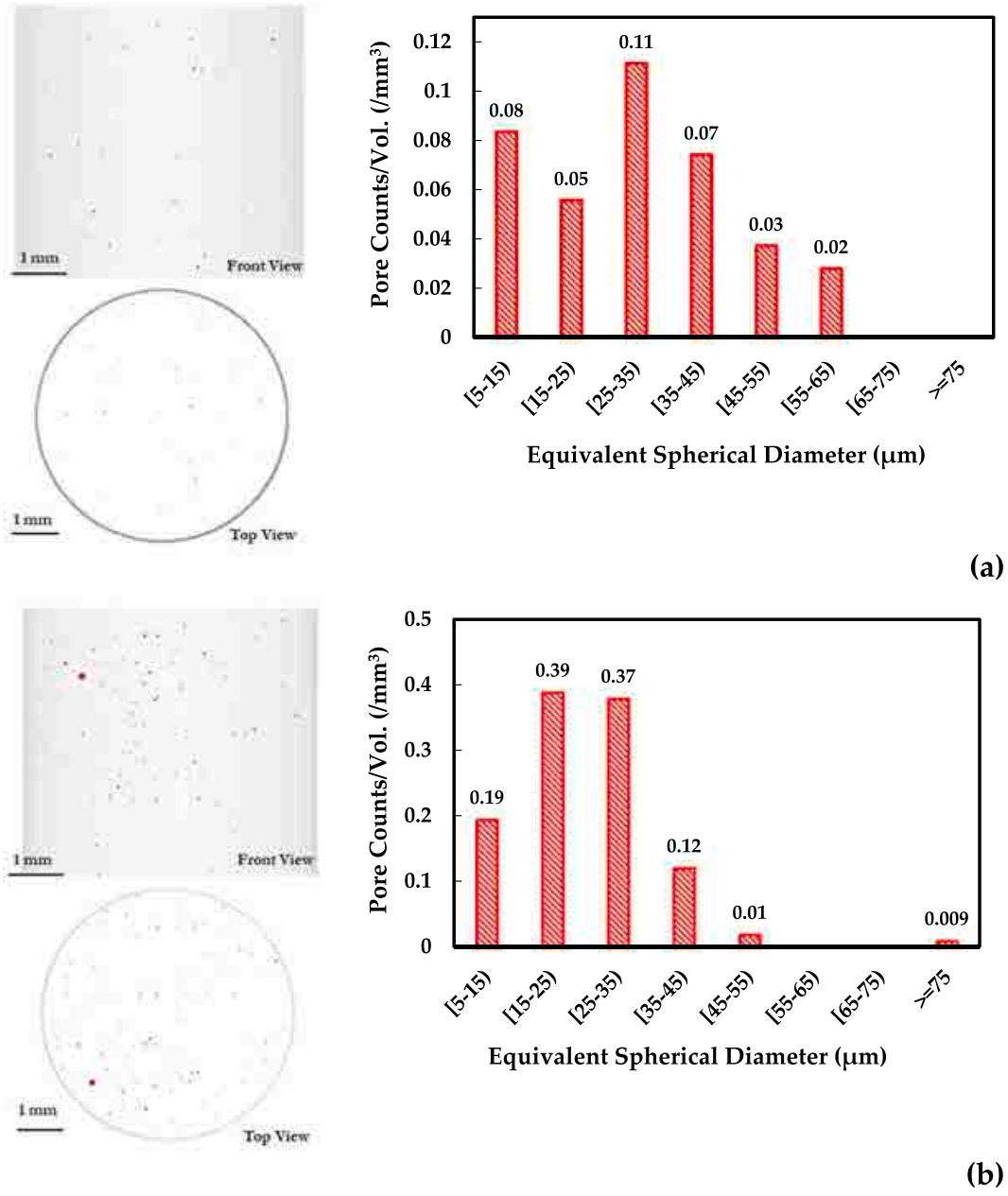

Fig. 6. μ-CT scan results showing defect distribution in (a) "runout" and (b) "untested" specimens.

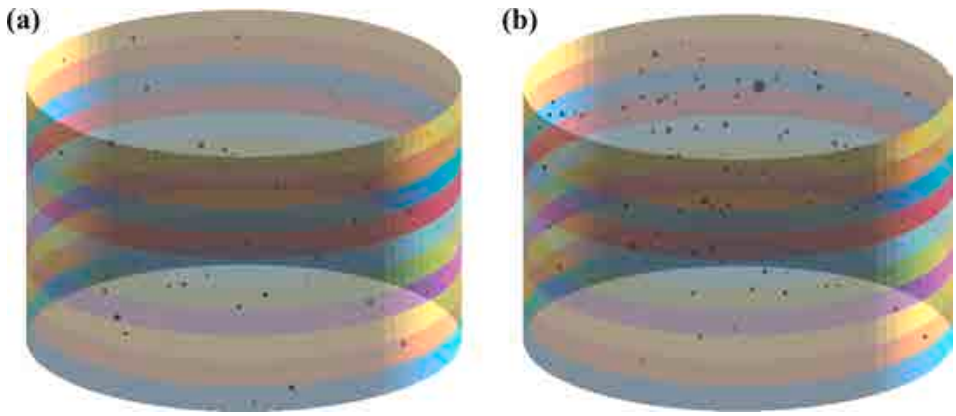

Fig. 7. Schematic illustration of volume division for the block maxima sampling from micro-CT results: (a) "runout" specimen; (b) "untested" specimen.

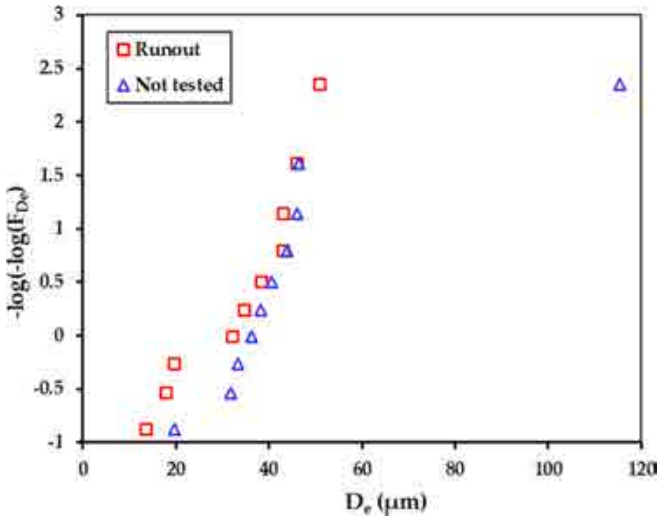

Fig. 8. Analysis of the statistical distribution of the equivalent diameters (D_e) on the Gumbel plot with estimated LEVD for the "runout" and the "untested" specimens.

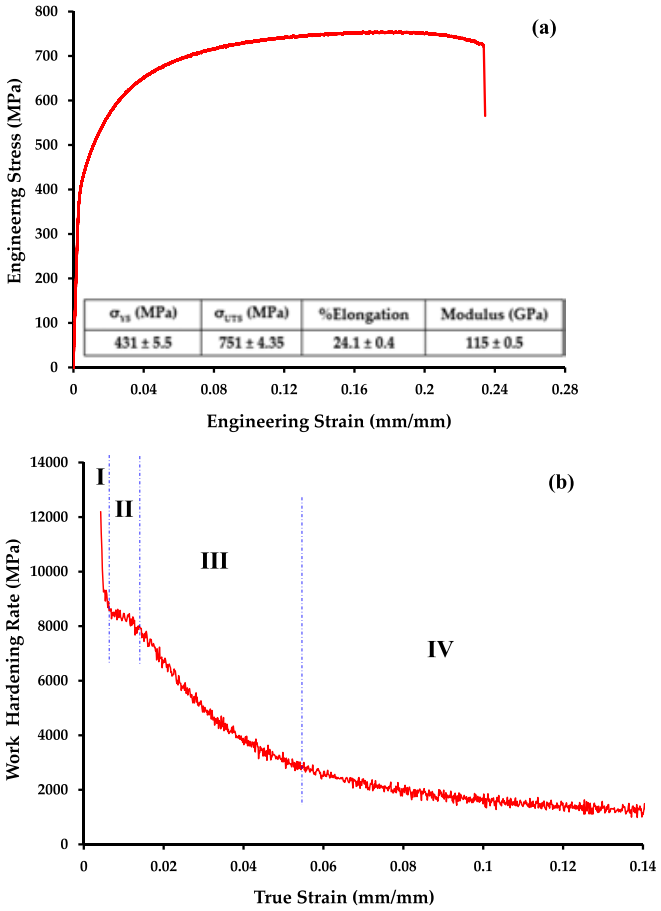

Fig. 9. (a) Engineering flow (stress–strain) curve of the studied annealed material; (b) the work hardening rate versus true strain curve.

microstructural changes occur, such as spheroidization and fragmentation of lamellar κ_{III} precipitates, coarsening and volume fraction reduction of finer κ_{IV} precipitates, and the precipitation of new needle-like κ_V intermetallic compounds. These alterations have been observed to enhance the static mechanical properties from the as-built to the annealed state [13,33]. These improved static properties may lead to better fatigue strength if the materials' fatigue behavior is not sensitive to the presence of volumetric defects [35,36].

The coarser and incoherent κ_{II} and κ_{III} particles have an accelerating effect on the fatigue crack growth rate [18,37]. This acceleration is due to the lattice mismatch between the matrix and the precipitate, which generates elastic strain in the surrounding matrix/precipitate interface. This strain hinders the movement of dislocations, resulting in the accumulation and pile-up of dislocations and a delay in the onset of yielding. Such dislocation interactions and accumulation around the aforementioned precipitates have been experimentally confirmed [38]. Therefore, these precipitates dominantly influence the strengthening of the material. However, the gradual accumulation of slip ultimately results in a localized increase in plastic strain along the interface, which promotes the initiation of cracks along the interface. Moreover, the continual plastic deformation occurring around the interface exacerbates the formation of voids. This phenomenon plays a pivotal role in further expediting the growth of cracks. The sustained plastic deformation induces localized stress concentrations, creating favorable conditions for void nucleation. As voids accumulate, they act as precursors to crack initiation and propagation [18]. As the nano-scale κ_{IV} precipitates are coherent with the matrix, their interactions with dislocations are different as compared to the κ_{II} and κ_{III} particles [38]. Dislocations can easily pass through the small and coherent precipitates and therefore they are weak obstacles to dislocation movement [39]. These coherent and shearable κ_{IV} precipitates provide less contribution to strengthening but their coherency with the matrix reduces elastic strain mismatch and thereby dislocation accumulation and pile-up are less likely for these precipitates which reduces the chance of crack initiation and greatly contributes to the ductility/toughness and better fatigue

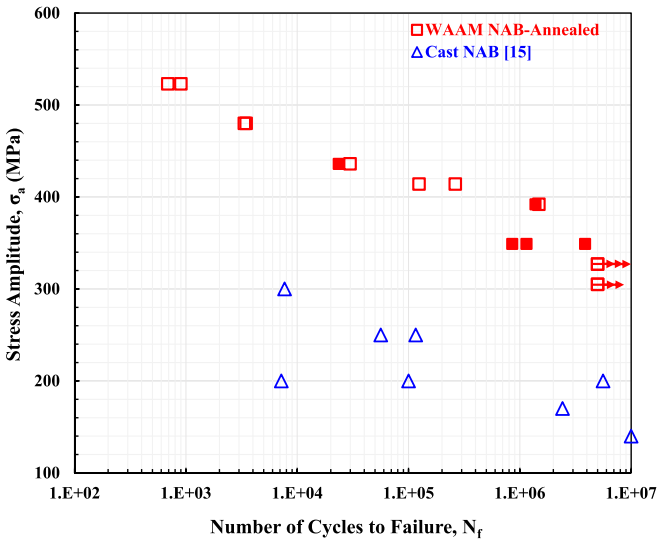

Fig. 10. S-N data for annealed WAAM NAB, in comparison with cast material [15]. Red hollow squares and red solid squares represent specimens that failed from surface and internal defects, respectively, while symbols with red arrows indicate runout specimens or fatigue strength at 5 million cycles. (For interpretation of the references to color in this figure legend, the reader is referred to the web version of this article.)

Table 3
S-N data with specimen ID and size of critical defects.

Specimen ID	Stress (MPa)	Number of cycles (N_f)	Defect size ($\sqrt{area}$) (μm)	Distance from surface to defect (μm)
F1	305	5.00E + 06 (Runout)	–	–
F2	305	5.00E + 06 (Runout)	–	–
F3	327	5.00E + 06 (Runout)	–	–
F4	327	5.00E + 06 (Runout)	–	–
F5	327	5.00E + 06 (Runout)	–	–
F6	349	3.86E + 06	~73 μm (internal)	~220 μm
F7	349	1.15E + 06	~86 μm (internal)	~280 μm
F8	349	8.54E + 05	~313 μm (internal)	~1890 μm
F9	392	1.48E + 06	Initiation from surface	0
F10	392	1.38E + 06	~80 μm (internal)	~270 μm
F11	414	2.63E + 05	Initiation from surface	0
F12	414	1.24E + 05	Initiation from surface	0
F13	436	2.98E + 04	Initiation from surface	0
F14	436	2.36E + 04	~181 μm (internal)	~570 μm
F15	480	3.48E + 03	Initiation from surface	0
F16	480	3.35E + 03	Initiation from surface	0
F17	523	9.01E + 02	Initiation from surface	0
F18	523	6.88E + 02	Initiation from surface	0

response of the material.

A microstructure featuring evenly dispersed, tiny, coherent precipitates distributed across the material leads to dislocation shearing activities with the localization of distinct planar dislocation structures (or planar bands) [37,38]. Such planar bands of dislocation result in a somewhat reversible glide process during cyclic loading [18,37]. This reversible slip/glide along these planes is said to mitigate fatigue crack growth by introducing tip deflection, causing crack closure, and mitigating damage accumulation, as suggested by previous studies [18,37,40,41].

3.2. Characteristics of volumetric defects

The micro-computed tomography (μ-CT) scan results, as shown in Fig. 6, provide a detailed glimpse into the internal defect structure of two fatigue specimens in the annealed condition – one tested and "runout" and one "untested". A total volume of 108 mm^3, with a voxel size of 5.5 μm, was scanned for each specimen. For the "runout" specimen, the scan unveiled 42 defects within the examined volume, characterized by a mean defect diameter of 30.6 μm and a maximum defect diameter reaching 64.6 μm. These findings underscore the density of the WAAM materials, as reflected in the minimal presence of defects (~99.99 % relative density). Conversely, the "untested" specimen unveiled a total of 120 defects. The mean defect diameter for the "untested" specimen was measured at 25.3 μm, with the most significant defect reaching a size of 116.2 μm. This comparative analysis suggests that the fatigue testing process does not seem to contribute to an increased size of defects. However, the difference in defect size can be expected due to the large variability of defects typical of AM parts.

3.2.1. Defect analysis using extreme value distribution (EVD)

According to the literature and the experimental evidence, larger defects have a more adverse impact on fatigue strength. The average defect size does not allow us to properly investigate the influence of defects on the fatigue response, whereas the upper tail of the defect size distribution provides more relevant information in a structural integrity context. Several studies have therefore opted to use the Largest Extreme Value Distribution (LEVD) analysis for assessing the statistical distribution of maximum defect sizes and outlined comprehensive procedures for this purpose [42–45]. The equivalent diameter (i.e., the diameter of the defect when it is considered a sphere), D_e, is considered as a representation of the equivalent defect size in the following analyses. The cumulative distribution function (CDF, $F(x)$) of the LEVD for the investigated D_e parameter is reported in Eq. (1):

$$F(D_e) = exp\left[- exp\left(- \frac{D_e - \mu}{\beta} \right) \right] \quad (1)$$

where β is the scale parameter and μ is the location parameter. In a Gumbel plot, the LEVD CDF is linearized, with the Y-axis reporting the reduced variate or Gumbel variate:

$$Y = -ln(- ln(F(D_e)) = \frac{D_e - \mu}{\beta} \quad (2)$$

A block maxima sampling [46,47] has been adopted to present the data on the Gumbel plot and investigate the largest defects. In particular, the inspected micro-CT volume has been sliced into 10 sub-volumes, and in each sub-volume, the defect with the largest equivalent diameter has been identified. Fig. 7 shows the initial inspected volume subdivided into the sub-volumes, with the defects schematically represented as spherical markers with their size being proportional to their equivalent diameter (Fig. 7a for the tested and runout specimen and Fig. 7b for the untested specimen).

The Gumbel plot of the defects identified from the block maxima sampling in terms of their equivalent diameters for the "runout" and the "untested" specimens are shown in Fig. 8. It can be noticed that the

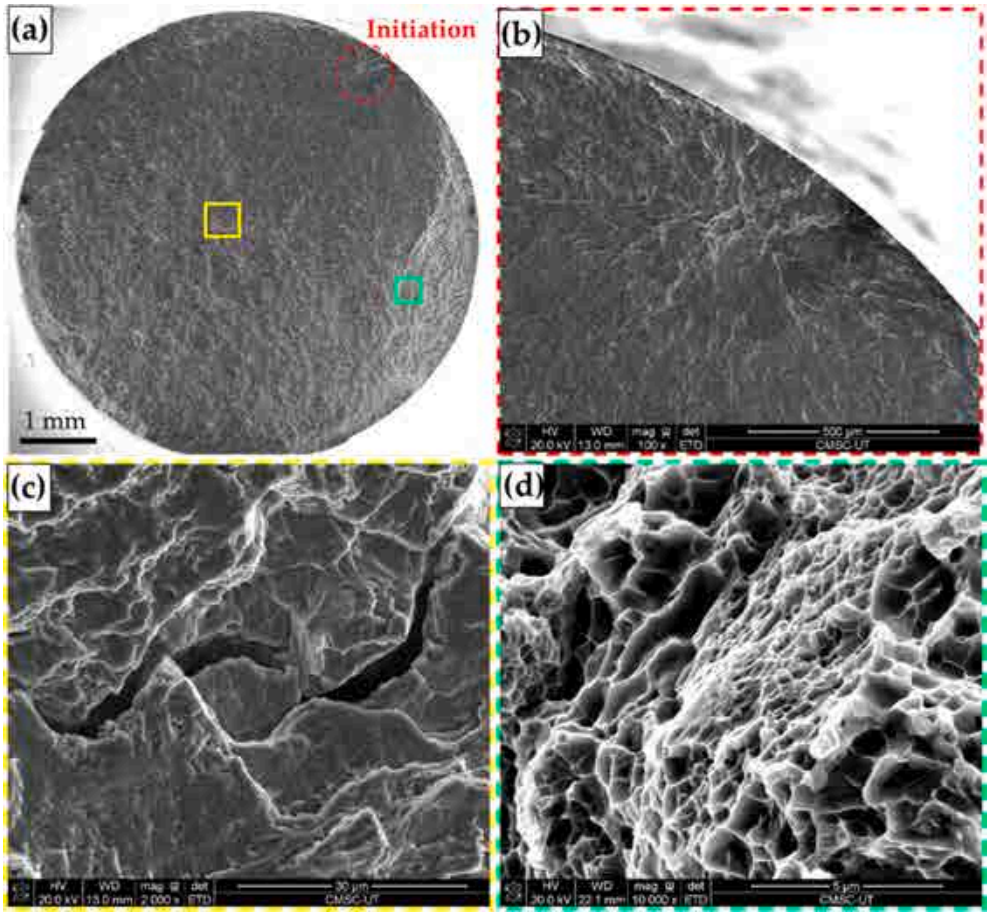

Fig. 11. The fracture surface of specimen F6 ($\sigma_a = 349$ MPa and $N_f = 3.86 \times 10^6$ cycles): (a) overview of the fracture surface, (b) initiation site (fisheye), (c) matrix cracking in the propagation region, and (d) mixture of fine and coarse dimples in the final fracture region.

experimental data do not significantly differ between the "runout" and the "untested" specimens. Indeed, the experimental defects follow the same trend with limited differences. However, a large defect with an equivalent diameter above 100μm has been found in the "untested" sub-volumes. The D_e of this defect is about twice the D_e of the largest defect found in the "runout" specimen. This rare and large defect is the one controlling the fatigue response, if present in the loaded volume during a fatigue test or in a component in in-service condition. It can be thus concluded that the defect size distribution in the "runout" and the "untested" specimens do not significantly differ: the defect size does not grow during a runout test. However, this analysis has interestingly pointed out that, even if defects are characterized by an equivalent diameter smaller than 60μm, rare and large defects with size above 100μm can be present and can significantly affect the fatigue response, contributing to the experimental scatter of the fatigue response typical of additively manufactured specimens.

3.3. Tensile (flow and work hardening) behavior

The average flow curve, the corresponding average values of yield strength (YS), ultimate tensile strength (UTS), elongation, and Young's modulus from three tensile tests are reported in Fig. 9. As reported in the literature, the YS and UTS of cast NAB, in the range of ~ 300 MPa and ~ 600 MPa, respectively, are much lower than the WAAM NAB material due to faster cooling/solidification in the WAAM process and the resulting finer grains/precipitates [4,17]. For as-built WAAM NAB, YS values of 388 MPa [13] and 328 MPa [38] were reported in the previous studies. Dharmendra et al. [13] reported 413 MPa as the YS for annealed (675 °C for 6 h) WAAM NAB. The previously reported YS and UTS values [13,38,48,49] are lower than those found in this study. Nonetheless, the samples examined in studies [13,38] exhibit greater ductility compared to the samples in this study. The work-hardening behavior of the annealed WAAM NAB alloy exhibits a characteristic four-stage strain-hardening response, typical of face-centered cubic (FCC) materials with low stacking fault energy (SFE) [50–52]. In the initial Stage I, the strain-hardening rate experiences a sharp decrease, primarily attributed to dislocation-induced plastic deformation dominance. Subsequently, Stage II reveals a plateau, wherein at small strain values, dislocations rapidly multiply with increasing strain. It is proposed that the plateau in Stage II is linked to the initiation of numerous stacking faults (SFs) and deformation twins, indicative of SF- and twinning-induced plasticity [53–55]. As strain progresses, the strain-hardening rate decreases in stages III and IV. The grain size emerges as a pivotal factor influencing deformation mechanisms, encompassing slip, SFs, and twinning activities. A reduction in grain size (WAAM versus cast) impedes the occurrence of deformation twinning.

3.4. S-N data

Fig. 10 shows the stress-life (S-N) data from fully reversed uniaxial fatigue testing. The WAAM NAB specimens were tested between 70 % (305 MPa) and 120 % (523 MPa) of yield strength. In Fig. 10, red hollow squares represent specimens that failed from fatigue cracks initiating at the surface, while red solid squares indicate specimens that failed because of internal defects. The red arrows represent runout specimens, or the fatigue strength recorded at 5 million cycles, with the number of arrows indicating the number of runout tests performed. The S-N data from annealed WAAM NAB is compared to a cast material tested by

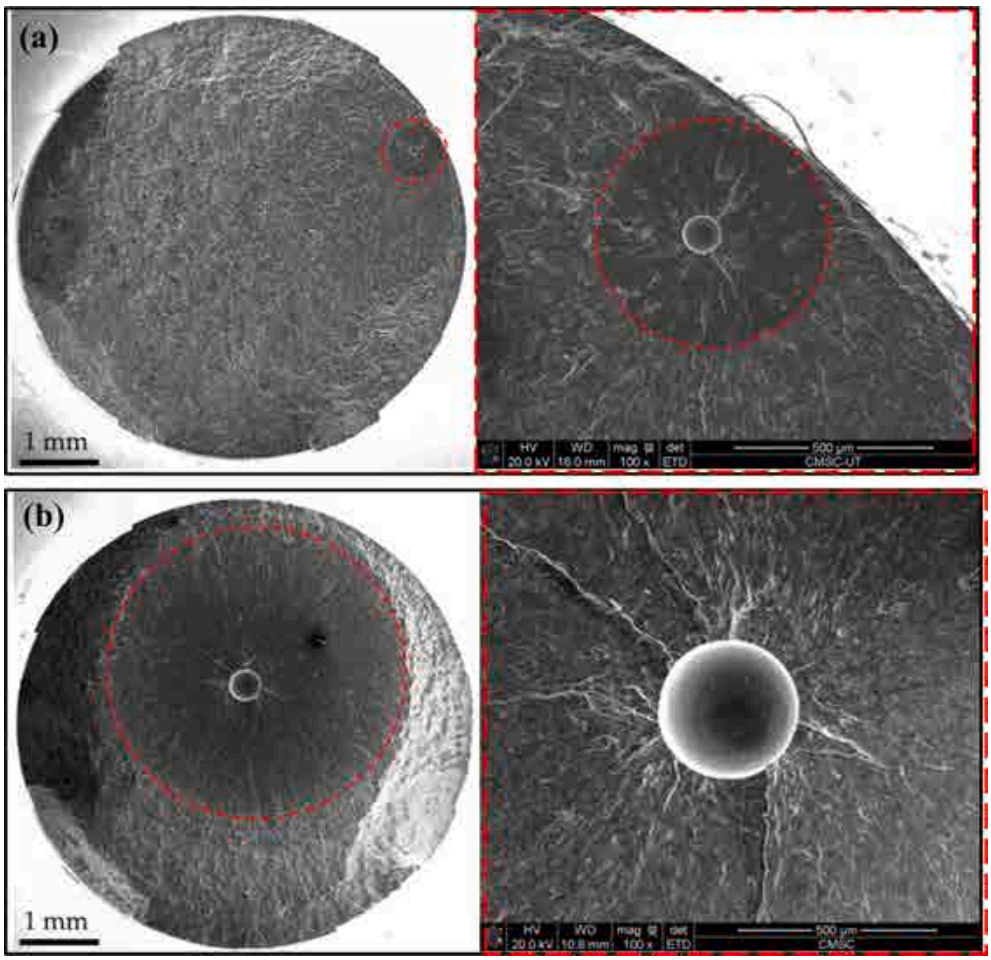

Fig. 12. The plane view of fracture surfaces and magnified view of the crack initiating defects for (a) specimen F7 ($\sigma_a = 349$ MPa and $N_f = 1.15 \times 10^6$ cycles) and (b) specimen F8 ($\sigma_a = 349$ MPa and $N_f = 8.54 \times 10^5$ cycles).

Sarkar et al. [15]. As shown in Fig. 10, the WAAM material exhibits a significantly higher fatigue strength at 5×10^6 cycles. Specimens that were tested at 70 % stress (305 MPa) and 75 % stress (327 MPa) showed no signs of fatigue failure even after 5 million cycles (i.e., runout). Consequently, it can be concluded that, at 5×10^6 cycles, the fatigue strength of the annealed WAAM NAB material exceeds 300 MPa.

The superior fatigue response of annealed WAAM NAB can be attributed to the considerable microstructural difference between cast and WAAM materials [13,34]. The microstructure of cast NAB contains brittle martensite β' phase with an acicular morphology and Fe_3Al-based large globular particles (i.e., κ_{III} phase); while in the WAAM NAB such phases are absent, due to the faster cooling rate of the process, and this contributes to better fatigue response of the WAAM material relative to the cast material. Annealing of as-WAAM material further modifies the microstructure, for instance, the authors studied the effect of post-WAAM annealing on the characteristics of intermetallic phases and reported the fragmentation and spheroidization of lamellar κ_{III} precipitates during post-annealing. The breakdown of κ_{III} lamellar phases results in the formation of multiple aligned and smaller particles as shown in our previous study [34]. The transformation of κ_{III} precipitates serves to mitigate the presence of sharp tips or terminals associated with the large lamella structure, thereby reducing stress concentrations, and promoting fatigue performance with a more homogenized distribution of stress throughout the material.

There is a significant difference between the literature data obtained by testing cast NAB and the WAAM NAB. The WAAM data are, indeed, significantly above the cast NAB data, with the estimated P-S-N curves following different trends and with a different overall slope, with the latter being higher for the cast NAB. This difference can be ascribed to the different defect sizes, which tended to be larger in the cast NAB [15] proving that WAAM NAB can be characterized by reasonably good fatigue performance. The WAAM NAB fatigue data exhibits scatter in the HCF regime but in the LCF regime, the data points cluster more tightly at each stress level. The exact stress amplitude and the corresponding number of cycles to failure are given in Table 3 with the specimens' codes and the size of the critical defect initiating fatigue crack. The table also reports the distance of the internal defects from the surface and helps understand the correlation between the defect size, location, stress amplitude, and fatigue life. The reason behind the scatters is comprehensively explored in the following subsection through SEM-based fractography.

3.5. Fractography analysis

In this section, we present SEM-based fractography analyses performed on the fractured specimens. The minimum stress level at which specimens failed is 349 MPa, with three specimens failing at this stress level, indicating notable variability in fatigue life (refer to S-N plot in Fig. 10). Fractography inspection on these three specimens is presented to uncover the cause of the scatter in S-N data. Fig. 11 shows the fracture surface of specimen F6 (349 MPa stress amplitude and 3.86×10^6 cycles to failure, from Table 3). In Fig. 11a, key features include marked initiation site, propagation region, and the locations of different high-magnification images. Fig. 11b displays a distinctive fisheye formation at the initiation site. Matrix cracking was evident at multiple locations in the propagation region, with a representative site shown from the

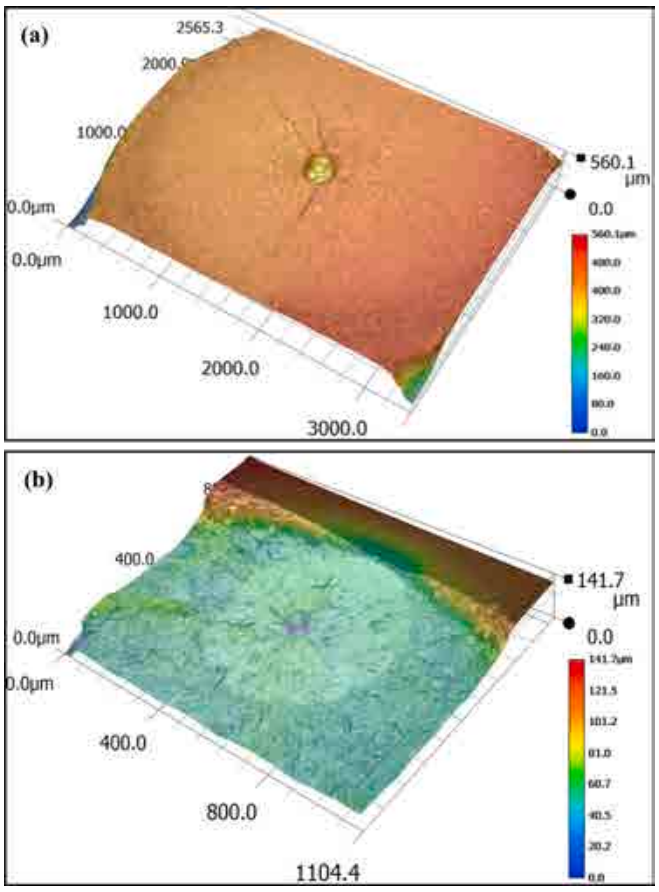

Fig. 13. Analysis of the circular feature observed at the center of fisheye: 3D depth profilometry on (a) specimen F8, and (b) specimen F10.

middle of the specimen (Fig. 11c). The final fracture region exhibits a combination of fine and coarse dimples (Fig. 11d), which is a consistent characteristic across all observed specimens and indicative of the ductile nature of the failure.

At the same stress level of 349 MPa, specimens F7 and F8 exhibited significantly shorter fatigue lives compared to specimen F6 (refer to Table 3 for the exact number of cycles). The fractured surfaces of these specimens are shown in Fig. 12. It is observed that the fracture surface of both F7 and F8 features a distinct fisheye pattern at the initiation site. Specifically, the initiation site for F7 is close to the surface (as shown in Fig. 12a), while for F8, it is located near the center of the specimen (as shown in Fig. 12b). Furthermore, when examined at the same magnification, the overall area of the fisheye and the defect at its core are significantly smaller in F7 than in F8. The size of the defect at the center of the fisheye is measured as $\sqrt{area}$ using ImageJ software. For specimen F6, the critical defect (the crack-initiating defect at the fisheye's center) is almost rectangular (refer to Fig. 11b), while it is circular for specimens F7 and F8. The size of the critical defect, measured as $\sqrt{area}$, is approximately 73 µm for F6, 86 µm for F7, and 313 µm for F8. Therefore, the scatter in fatigue life is driven by the size of the critical defect at this stress level. Also, it is important to note that the location of the defect has significantly influenced the fatigue life. For example, for specimens F6 and F7, the defect location is near the surface and a slight increase in defect size significantly reduced the fatigue life, whereas a significantly larger defect located at the center of specimen F8 did not reduce fatigue life as dramatically.

The circular feature at the center of the fisheye is commonly observed on many specimens and under the SEM, it looks like a spherical particle. This is further investigated by optical microscopy-based 3D depth profilometry, as shown in Fig. 13a&b, for specimens F8 and F10. The profilometry images, with their color-coded depth scales, clearly reveal that the circular feature dips below the surface, confirming that the feature at the center of the fisheye is a process-induced pore.

Fractography analysis on all fracture surfaces shows that at lower stress levels, such as at 349 MPa and 392 MPa, failure primarily begins from internal defects. When the stress increases to 414 MPa, the point of failure shifts to the surface for specimens F11 and F12, as evidenced in Fig. 14a&b. Despite some variability in fatigue life at 414 MPa, (refer to the S-N plot in Fig. 10 or Table 3), the initiation site remains consistent, with both specimens exhibiting surface-based failure initiation without the influence of defects. At elevated stress of 436 MPa, specimen F14 presents fisheye formation again, as depicted in Fig. 14c. The magnified view of the fisheye core in Fig. 14c, clearly shows that there is a large spherical defect (i.e., a pore) at the center with defect size ($\sqrt{area}$) ~ 45 µm and numerous small pores in the white rough area (WRA) surrounding the large spherical pore (the measured $\sqrt{area}$ of the WRA is ~ 181 µm). This observation suggests that the core of the fisheye has a lack of fusion defect and the presence of such a large internal defect led to internal failure at the elevated stress level of 436 MPa. Conversely, at the stress level of 414 MPa, both specimens F11 and F12 experienced surface-based crack initiation (Fig. 14a&b), likely due to the absence of sufficiently large defects to trigger internal failure, making the surface the most vulnerable region.

For all specimens tested above a stress level of 436 MPa, crack initiation is from the surface. At high-stress levels, such as the maximum stress of 523 MPa (which is 120 % of YS), the specimens exhibit multiple crack initiation sites on the specimen surfaces, which contrasts with the singular crack initiation sites observed at lower or moderate stress levels. Detailed fractography for specimen F18, which failed at 523 MPa, is shown in Fig. 15 as a representative of the fracture morphology in high-stress levels. Fig. 15a&b shows the overall fracture surface and part of the initiation area. Secondary cracks are detected in the propagation area, as shown in Fig. 15c, along with fine rubbing marks (both indicated by yellow arrows). A combination of fine and coarse dimples dominates the morphology of the final fracture region; however, occasionally some flat areas with rubbing marks are observed in the final fracture region, as shown in Fig. 15d.

The detailed fractographic analysis demonstrated that the initiation of fatigue cracks in the material under study is not exclusively linked to defects. Instead, fatigue failure can be defect-driven or microstructure-driven. At low-stress levels, the observation underscores that the fatigue performance is sensitive to the presence, size, and location of defects, while at high-stress levels, failure starts from single or multiple locations from the surface without any influence of defects. This confirmed that this material is not solely sensitive to defects in its fatigue behavior. For this reason, the enhanced static properties in WAAM NAB (due to microstructure refinement) could contribute to better fatigue strength. This is in contrast to certain defect-sensitive materials [56,57], such as 17-4 PH stainless steel [58], whose fatigue strength deteriorated after aging treatment. For 17-4 PH stainless steel [58], fatigue cracks started at un-melted areas, such as inter-layer cavities/voids for all conditions, identified as particularly harmful due to their size and irregular shape, leading to higher stress concentrations compared to spherical pores.

3.6. Fatigue-induced deformed microstructure

To analyze the fatigue deformation two annealed NAB specimens (from the HCF and LCF region) that failed from fatigue loading were sectioned in the loading directions. The process of preparing cross-sectional samples from the fatigue-fractured specimens using EDM wire cut is illustrated in a schematic diagram shown in Fig. 16, along with the crack initiation site and the target area for EBSD scanning. The two samples are coded as F7 ($\sigma_a = 349$ MPa, and $N_f = 1.15 \times 10^6$ cycles) and F18 ($\sigma_a = 523$ MPa, and $N_f = 6.88 \times 10^2$ cycles).

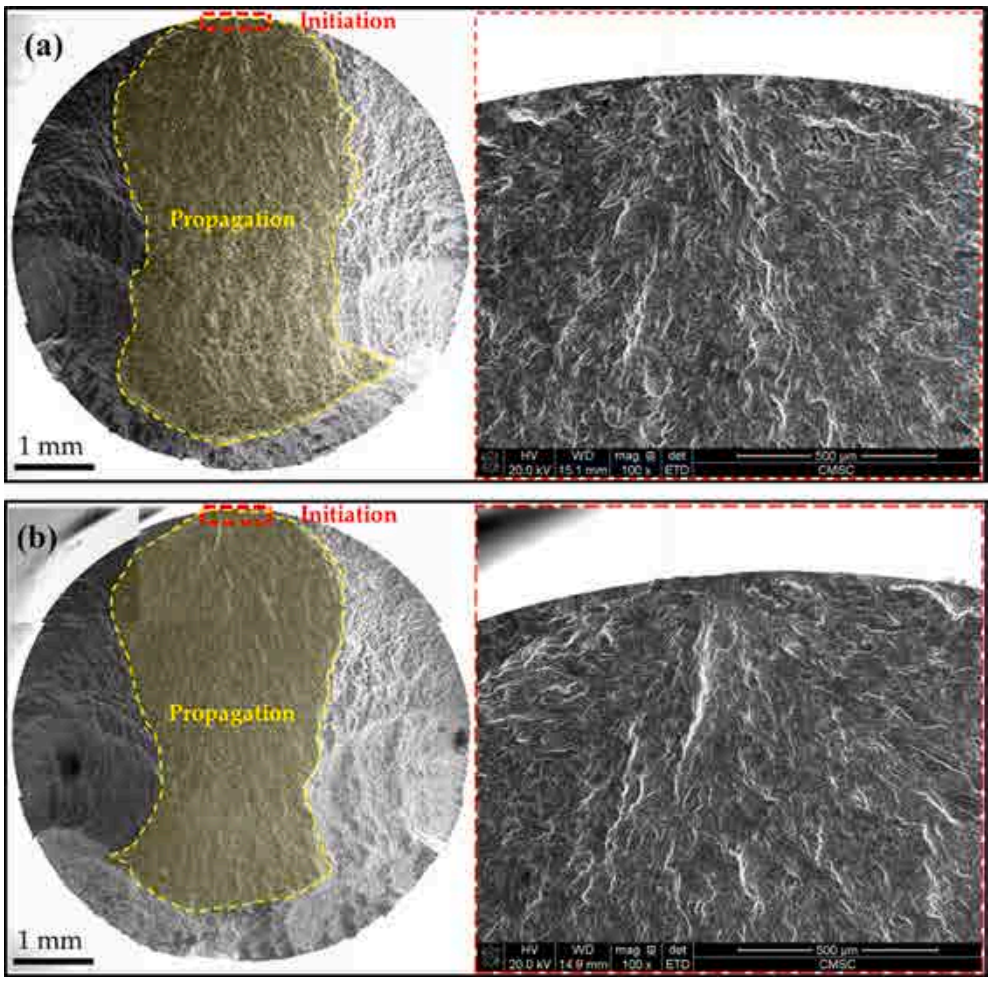

Fig. 14. Overall fracture surface and crack initiation site on (a) specimen F11 ($\sigma_a = 414$ MPa, and $N_f = 2.63 \times 10^5$ cycles), (b) specimen F12 ($\sigma_a = 414$ MPa, and $N_f = 1.24 \times 10^5$ cycles), and (c) specimen F14 ($\sigma_a = 436$ MPa, and $N_f = 2.36 \times 10^4$ cycles).

The data obtained from the EBSD scan was utilized to construct localized discrepancies in strain between the α-grain and its surrounding regions, employing the KAM, to gain a better understanding of the deformation behavior at low and high-stress levels that causes defect-driven and microstructure-driven failure respectively. The KAM map illustrates the mean misorientation angle of a specific point concerning its three closest neighbors. An elevated KAM value denotes a greater local crystal misalignment, signifying developed plastic strain within the material. Based on the KAM maps shown in Fig. 17, highly dense misorientations are in the vicinity of the fracture surface for both samples, but the overall density is slightly higher for the HCF specimen (i.e., F7). The correlation between KAM distribution and the deformation map is shown in Fig. 18, where the fraction of deformed grains (which is a plastic wake region and contains more dislocations) diminished in the same manner as elevated misorientation (i.e., the larger density of high angle grain boundaries) in Fig. 17.

The deformation maps shown in Fig. 18 visualize the deformed, substructured, and recrystallized grains in red, yellow, and blue colors, respectively. The grains are distinguished according to the internal average misorientation angles (IAMA) of the grains calculated from EBSD data. Deformed regions are grains with IAMA greater than 1°, whereas those with IAMA below 1° are categorized as recrystallized grains. Substructured grains have an average angle of less than 1°, but their subgrain-to-subgrain misorientation angle exceeds 1° [59,60]. As seen in Fig. 17, deformed grains (this plastically deformed area is known as the plastic wake) are located near the fractured surface of both samples. The fraction of deformed grains is higher in the HCF specimen (Fig. 18a) compared to the LCF specimen (Fig. 18b). On the other hand, the substructured grains are higher in fraction for the LCF specimen. The presence of substructured grains may indicate the occurrence of localized plastic deformation zones, while such substructures can lead to strain localization and potential stress concentrations. The fraction of recrystallized grains is found almost the same in both samples. Recrystallized grains indicate that the material has undergone recrystallization, replacing deformed grains with new, strain-free grains. This often results in improved ductility, reduced hardness, and enhanced toughness. Recrystallized grains can lead to a more homogeneous and isotropic material, reducing anisotropy in mechanical properties. It is important to note that the accuracy of EBSD indexing in crack initiating/propagating region can impact the reliability of the conclusions drawn which can be challenging. As seen in Fig. 17&18, the indexing for sample F18 is not as good as F7. However, despite the limitations regarding the indexing, the presented EBSD analysis remains valuable for providing qualitative insights into the fatigue deformation behavior of the microstructure. The IAMA-based partitioning of the grains (i.e., recrystallized, substructured, and deformed) still offers relevant information, but interpretations should be taken with caution, taking into account the indexation quality and specific zones of observation.

4. Conclusions

In the present work, the fully reversed uniaxial fatigue response of

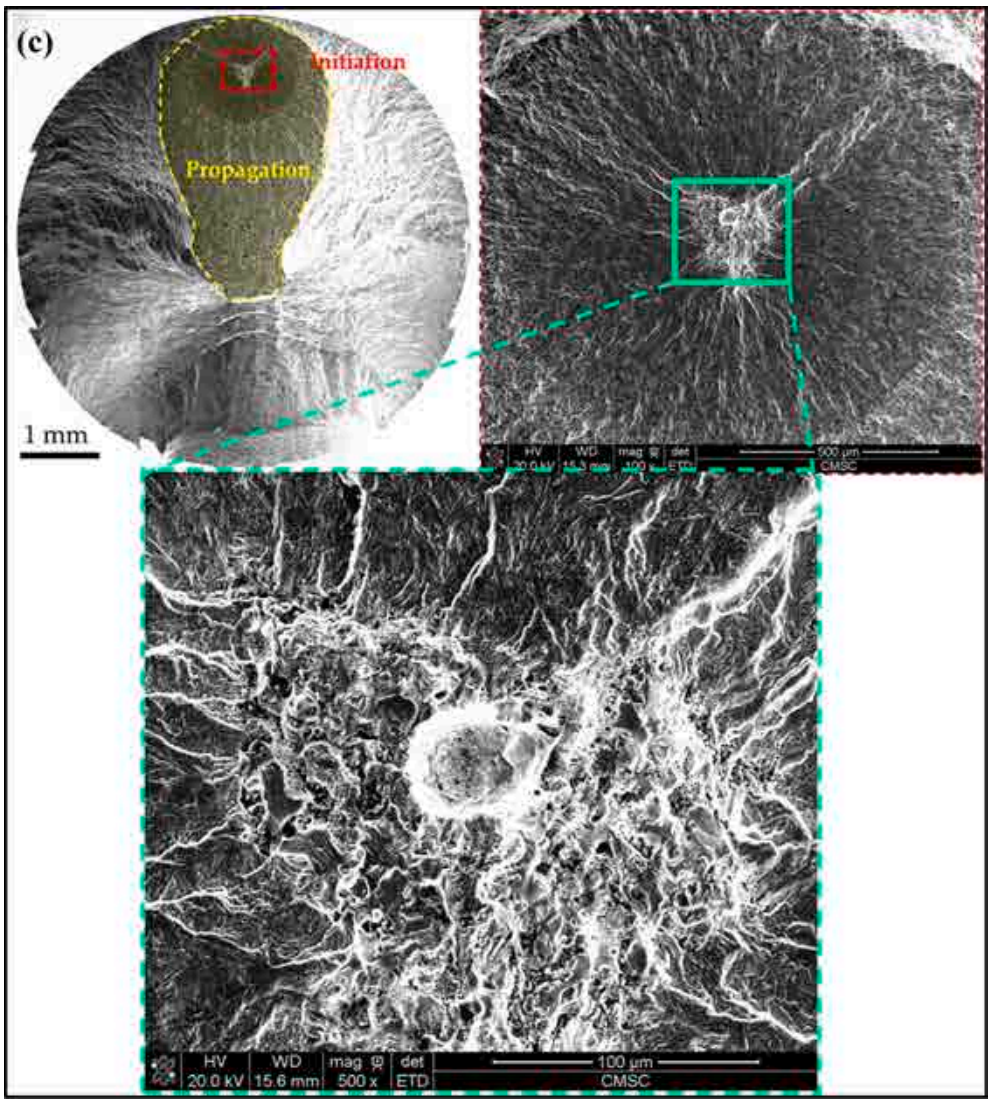

Fig. 14. (*continued*).

wire arc additive manufactured (WAAM) nickel-aluminum bronze (NAB) in the annealed condition (675 °C for 6 h) is investigated at room temperature. Tensile testing is conducted in parallel to understand the mechanical properties. The starting microstructure and fatigue-deformed microstructure of annealed samples are investigated by employing electron backscatter diffraction (EBSD) analysis. X-ray μ-CT scanning is utilized to analyze the defect distribution in the "runout" and "untested" fatigue specimens and the fractured specimens are investigated employing scanning electron microscopy (SEM) based fractography to understand the crack initiation and propagation characteristics. The results of the investigation yield the subsequent conclusions:

(i) The EBSD analysis of annealed WAAM NAB reveals a significantly reduced grain size relative to the cast counter material, averaging 2.46 ± 3.70 μm, attributed to the rapid solidification in the WAAM process. Texture analysis indicates a multiple random distribution (MRD) value of only 2.61, signifying a relatively weak or nearly random texture in the annealed microstructure.

(ii) The WAAM NAB specimens fabricated in this study are highly dense (~99.99 % density) with only a few microscopic defects revealed through μ-CT scans, which is credited to the well-developed process parameters.

(iii) The tensile properties in the present study, with a yield strength (YS) of 431 MPa and ultimate tensile strength (UTS) of 751 MPa, notably surpass those reported for the as-built condition in prior studies and slightly outperform those observed in heat-treated conditions.

(iv) The annealed WAAM NAB material demonstrates remarkably higher fatigue strength, surpassing 300 MPa at 5×10^6 cycles, and notably outperforms the cast material in fully reversed uniaxial fatigue testing.

(v) Fractographic analysis reveals that fatigue crack initiation is not entirely defect-dependent; it can be influenced by either defects or microstructural characteristics. The material's fatigue performance is notably affected by the size and location of the internal defects at low-stress levels, but at higher stresses, failure can begin from surface areas independently of defects and driven by microstructure. Therefore, the failure mechanism shifts from internal initiation to surface-based mechanisms with the increase of stress.

(vi) EBSD analysis of fatigue-deformed samples under both low- and high-stress levels showed variations in localized strain and the proportion of deformed grains near the fracture surface, with the sample subjected to low stress displaying a marginally greater extent of both, resulting in an expanded plastic wake region.

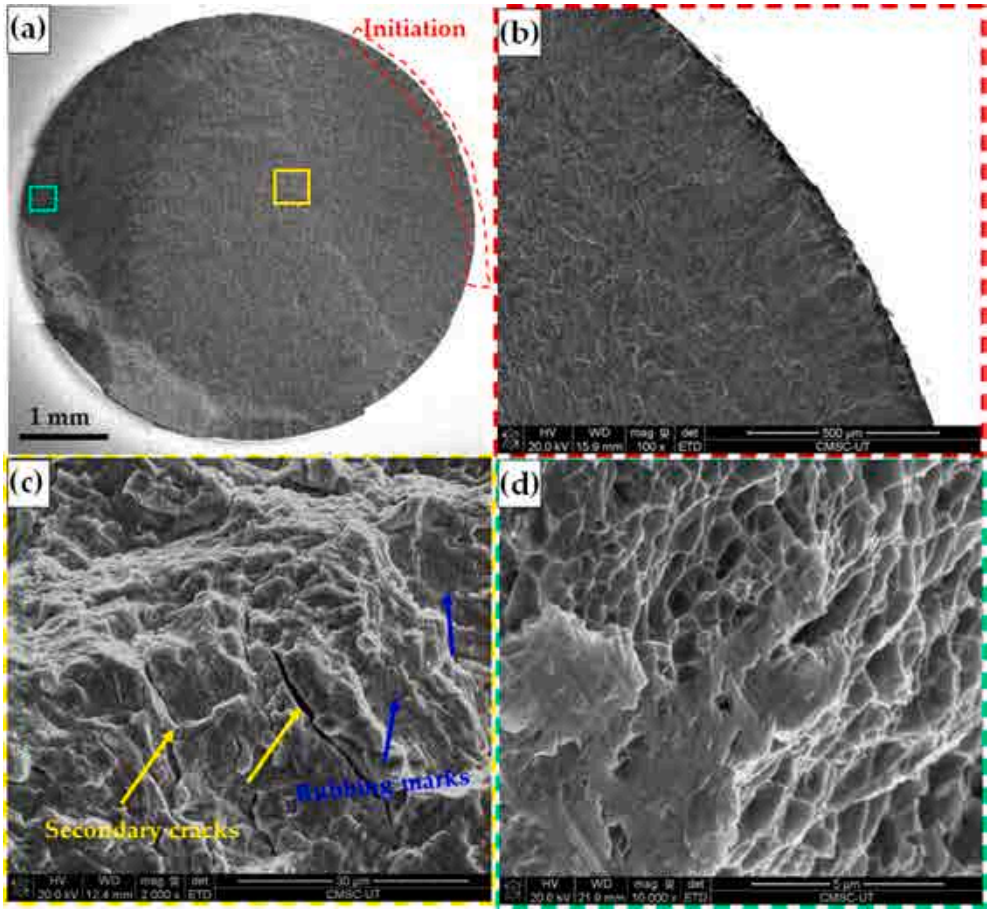

Fig. 15. The fracture surface of specimen F18 ($\sigma_a = 523$ MPa, and $N_f = 6.88 \times 10^2$ cycles): (a) overview of the fracture surface, (b) initiation site, (c) propagation region with the presence of secondary cracks and fine rubbing marks, and (d) mixture of the flat zone with rubbing marks and dimpling in the final fracture region.

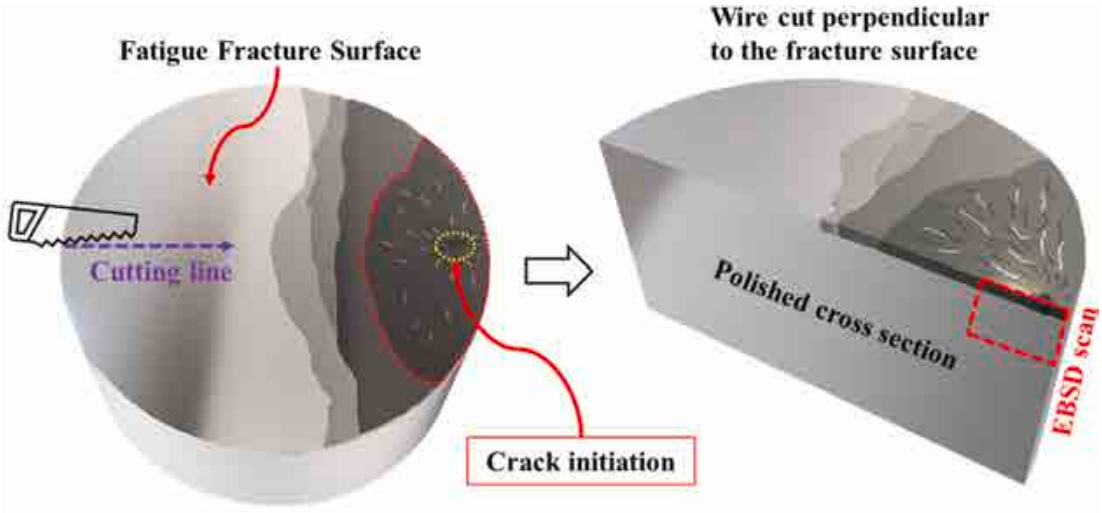

Fig. 16. Illustrative representation of the fractured sample detailing the crack initiation site, EDM wire cutting path, and the target area for EBSD analysis on the vertically sectioned surface.

CRediT authorship contribution statement

Shawkat I. Shakil: Writing – original draft, Methodology, Investigation, Formal analysis, Data curation. **Sajad Shakerin:** Methodology, Investigation, Formal analysis. **Keivan Rahmdel:** Methodology, Investigation, Formal analysis. **Mohsen Mohammadi:** Writing – review & editing, Resources, Data curation. **Andrea Tridello:** Writing – review & editing, Validation, Software, Methodology, Formal analysis. **Davide S. Paolino:** Writing – review & editing, Validation, Investigation, Formal analysis. **Shuai Shao:** Writing – review & editing, Formal analysis. **Nima Shamsaei:** Writing – review & editing, Validation, Resources. **Meysam Haghshenas:** Supervision, Resources, Project administration,

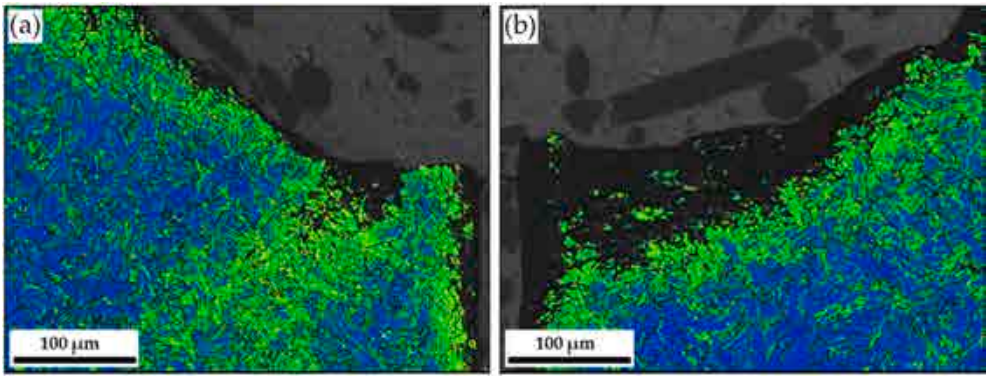

Fig. 17. Kernel average misorientation (KAM) for (a) F7, and (b) F18.

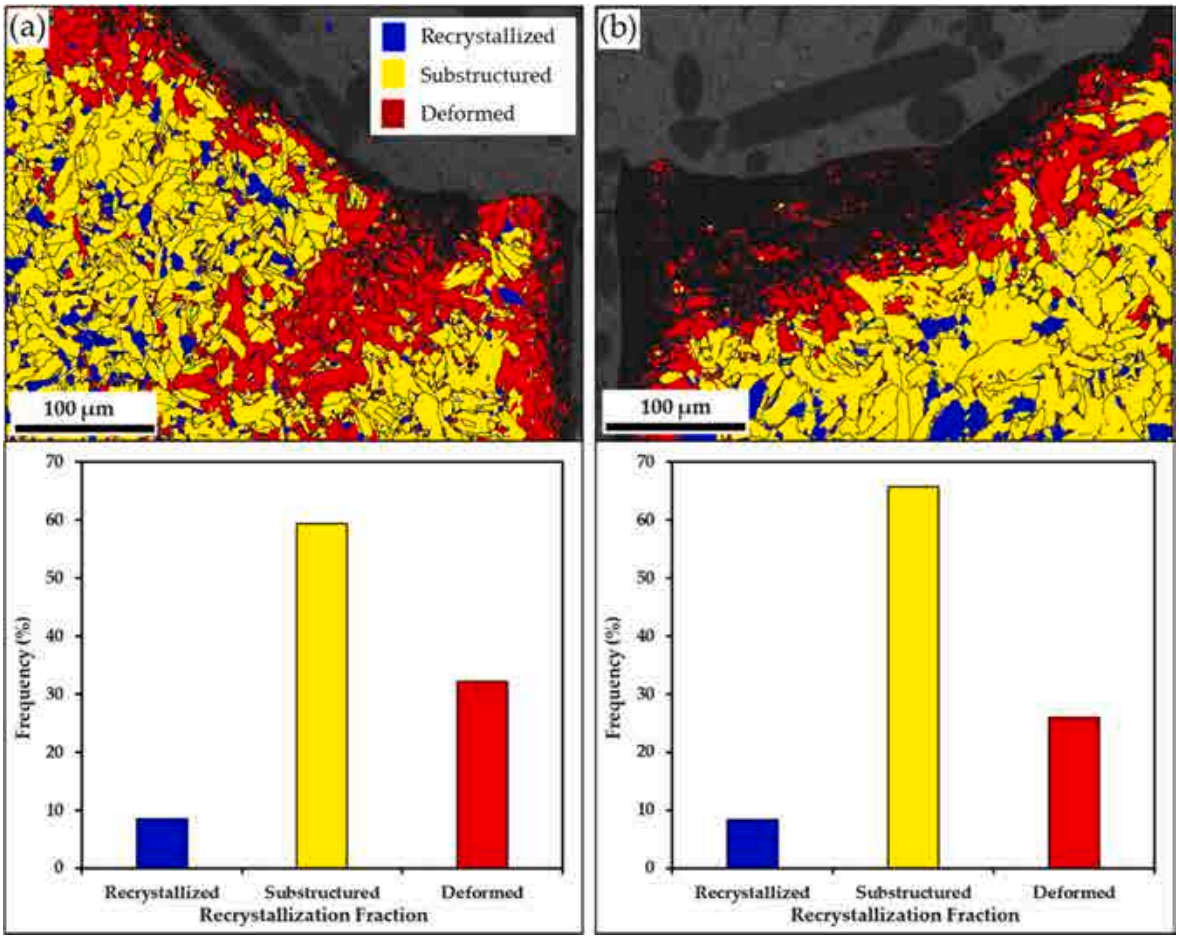

Fig. 18. Deformation map and fraction of recrystallized, substructured, and deformed grains beneath the region where the crack initiates on the fracture surface of (a) F7, and (b) F18.

Funding acquisition, Conceptualization.

Declaration of competing interest

The authors declare that they have no known competing financial interests or personal relationships that could have appeared to influence the work reported in this paper.

Data availability

Data will be made available on request.

Acknowledgment

The corresponding author expresses gratitude for the financial support provided by the Office of Naval Research (ONR) through grant number N00014-23-1-2798. The last author also acknowledges the significant contributions of Dr. Mark Douglass and Mr. Ben Schaeffer from Lincoln Electric Additive Solutions (LEAS) for their valuable discussions and assistance in printing the NAB walls.

References

[1] Treutler K, Wesling V. The current state of research of wire arc additive manufacturing (WAAM): a review. Appl Sci 2021;11(18):8619.
[2] Cunningham CR, Flynn JM, Shokrani A, Dhokia V, Newman ST. Invited review article: strategies and processes for high quality wire arc additive manufacturing. Addit Manuf 2018;22:672–86.
[3] Richardson I. Guide to nickel aluminium bronze for engineers. Copper Development Association; 2016.
[4] Dharmendra C, Hadadzadeh A, Amirkhiz BS, Janaki Ram GD, Mohammadi M. Microstructural evolution and mechanical behavior of nickel aluminum bronze Cu-9Al-4Fe-4Ni-1Mn fabricated through wire-arc additive manufacturing. Addit Manuf 2019;30:100872.
[5] Xu C, Peng Y, Chen L-Y, Zhang T-Y, He S, Wang K-H. Corrosion behavior of wire-arc additive manufactured and as-cast Ni-Al bronze in 3.5 wt% NaCl solution. Corros Sci 2023;215:111048.
[6] Behvar A., Haghshenas M. A critical review on very high cycle corrosion fatigue: mechanisms, methods, materials, and models. J Space Safety Eng 10(3) 2023:284-323.
[7] Anantapong J, Uthaisangsuk V, Suranuntchai S, Manonukul A. Effect of hot working on microstructure evolution of as-cast Nickel Aluminum Bronze alloy. Mater Des 2014;60:233–43.
[8] Orzolek SM, Semple JK, Fisher CR. Influence of processing on the microstructure of nickel aluminum bronze (NAB). Addit Manuf 2022;102859.
[9] Nelson EA. Microstructural effects of multiple passes during friction stir processing of nickel aluminum bronze, Naval Postgraduate School Monterey Ca, 2009.
[10] Ou W, Mukherjee T, Knapp GL, Wei Y, DebRoy T. Fusion zone geometries, cooling rates and solidification parameters during wire arc additive manufacturing. Int J Heat Mass Transf 2018;127:1084–94.
[11] Gudur S, Nagallapati V, Pawar S, Muvvala G, Simhambhatla S, A study on the effect of substrate heating and cooling on bead geometry in wire arc additive manufacturing and its correlation with cooling rate, Mater Today: Proc 2021; 41: 431-436.
[12] Dharmendra C, Hadadzadeh A, Amirkhiz BS, Ram GDJ, Mohammadi M. Microstructural evolution and mechanical behavior of nickel aluminum bronze Cu-9Al-4Fe-4Ni-1Mn fabricated through wire-arc additive manufacturing. Addit Manuf 2019;30:100872.
[13] Dharmendra C, Amirkhiz BS, Lloyd A, Ram GDJ, Mohammadi M. Wire-arc additive manufactured nickel aluminum bronze with enhanced mechanical properties using heat treatments cycles. Addit Manuf 2020;36:101510.
[14] Chakrabarti A, Sarkar A, Saravanan T, Nagesha A, Sandhya R, Jayakumar T. Influence of mean stress and defect distribution on the high cycle fatigue behaviour of cast Ni-Al bronze. Proc Eng 2014;86:103–10.
[15] Sarkar A, Chakrabarti A, Nagesha A, Saravanan T, Arunmuthu K, Sandhya R, et al. Influence of casting defects on S-N fatigue behavior of Ni-Al bronze. Metall Mater Trans A 2015;46:708–25.
[16] Lahiri BB, Sarkar A, Bagavathiappan S, Nagesha A, Saravanan T, Sandhya R, et al. Studies on temperature evolution during fatigue cycling of Ni-Al bronze (NAB) alloy using infrared thermography. Insight-Non-Destructive Test Cond Monit 2016; 58(2):70–81.
[17] Lv Y, Hu M, Wang L, Xu X, Han Y, Lu W. Influences of heat treatment on fatigue crack growth behavior of NiAl bronze (NAB) alloy. J Mater Res 2015;30(20): 3041–8.
[18] Xu X, Lv Y, Hu M, Xiong D, Zhang L, Wang L, et al. Influence of second phases on fatigue crack growth behavior of nickel aluminum bronze. Int J Fatigue 2016;82: 579–87.
[19] Gao Y, Yang W, Huang Z, Lu Z. Effects of residual stress and surface roughness on the fatigue life of nickel aluminium bronze alloy under laser shock peening. Eng Fract Mech 2021;244:107524.
[20] Ding Y, Lv Y, Zhao B, Han Y, Wang L, Lu W. Response relationship between loading condition and corrosion fatigue behavior of nickel-aluminum bronze alloy and its crack tip damage mechanism. Mater Charact 2018;144:356–67.
[21] Mshana JS, Vosikovsky O, Sahoo M. Corrosion fatigue behaviour of nickel-aluminum bronze alloys. Can Metall Q 1984;23(1):7–15.
[22] Lv Y, Nie B, Wang L, Cui H, Li L, Wang R, et al. Optimal microstructures on fatigue properties of friction stir processed NiAl bronze alloy and its resistant fatigue crack growth mechanism. Mater Sci Eng A 2020;771:138577.
[23] Dharmendra C, Hadadzadeh A, Amirkhiz BS, Mohammadi M. The morphology, crystallography, and chemistry of phases in wire-arc additively manufactured nickel aluminum bronze, Springer, pp. 443-453.
[24] Dharmendra C, Gururaj K, Pradeep KG, Mohammadi M. Characterization of κ-precipitates in wire-arc additive manufactured nickel aluminum bronze: A combined transmission Kikuchi diffraction and atom probe tomography study. Addit Manuf 2021;46:102137.
[25] Ding D, Pan Z, Van Duin S, Li H, Shen C. Fabricating superior NiAl bronze components through wire arc additive manufacturing. Materials 2016;9(8):652.
[26] Dharmendra C, Shakerin S, Ram GDJ, Mohammadi M. Wire-arc additive manufacturing of nickel aluminum bronze/stainless steel hybrid parts–Interfacial characterization, prospects, and problems. Materialia 2020;13:100834.
[27] Shakil SI, Dharmendra C, Amirkhiz BS, Verma D, Mohammadi M, Haghshenas M. Micromechanical characterization of wire-arc additive manufactured and cast nickel aluminum bronze: Ambient and intermediate temperatures. Mater Sci Eng A 2020;792:139773.
[28] Bercelli L, Moyne S, Dhondt M, Doudard C, Calloch S, Beaudet J. A probabilistic approach for high cycle fatigue of Wire and Arc Additive Manufactured parts taking into account process-induced pores. Addit Manuf 2021;42:101989.
[29] Bercelli L, Doudard C, Calloch S, Le Saux V, Beaudet J. Thermometric investigations for the characterization of fatigue crack initiation and propagation in Wire and Arc Additively Manufactured parts with as-built surfaces. Fatigue Fract Eng Mater Struct 2023;46(1):153–70.
[30] ASTM, E8/E8M Standard Test Methods of Tension Testing of Metallic Materials, American Society for Testing and Materials, Annual Book or ASTM Standards, 2013.
[31] ASTM, E466 Standard Practice for Conducting Constant Amplitude Axial Fatigue Tests of Metallic Specimens, American Society for Testing and Materials, Annual Book or ASTM Standards, 2021.
[32] Kuppahalli P, Keshavamurthy R, Sriram P, Kavya JT. Microstructural and mechanical behaviour of nickel aluminum bronze alloys, IOP Publishing, p. 012044.
[33] Shen C, Pan Z, Ding D, Yuan L, Nie N, Wang Y, et al. The influence of post-production heat treatment on the multi-directional properties of nickel-aluminum bronze alloy fabricated using wire-arc additive manufacturing process. Addit Manuf 2018;23:411–21.
[34] Shakil SI, Dharmendra C, Shalchi-Amirkhiz B, Mohammadi M, Haghshenas M. Interplay between microstructure, micromechanical, and tensile properties in wire arc additive manufactured nickel-aluminum bronze: As-built and heat treated. Materialia 2023;32:101919.
[35] Dodaran MS, Muhammad M, Shamsaei N, Shao S. Synergistic effect of microstructure and defects on the initiation of fatigue cracks in additively manufactured Inconel 718. Int J Fatigue 2022;162:107002.
[36] Muhammad M, Frye P, Simsiriwong J, Shao S, Shamsaei N. An investigation into the effects of cyclic strain rate on the high cycle and very high cycle fatigue behaviors of wrought and additively manufactured Inconel 718. Int J Fatigue 2021; 144:106038.
[37] Wang YL, Pan QL, Wei LL, Li B, Wang Y. Effect of retrogression and reaging treatment on the microstructure and fatigue crack growth behavior of 7050 aluminum alloy thick plate. Mater Des 2014;55:857–63.
[38] Murphy-Leonard A, Mazánová V. Uncovering dislocation-precipitate interactions during tensile loading of wire arc additive manufactured nickel-aluminum-bronze. MRS Commun 2023:1–7.
[39] Wang Q, Li Z, Pang S, Li X, Dong C, Liaw PK. Coherent precipitation and strengthening in compositionally complex alloys: a review. Entropy 2018;20(11): 878.
[40] Borrego LP, Costa JM, Silva S, Ferreira JM. Microstructure dependent fatigue crack growth in aged hardened aluminium alloys. Int J Fatigue 2004;26(12):1321–31.
[41] Csontos AA, Starke EA. The effect of inhomogeneous plastic deformation on the ductility and fracture behavior of age hardenable aluminum alloys. Int J Plast 2005;21(6):1097–118.
[42] Cheng M, Lu Z, Wu J, Guo R, Qiao J, Xu L, et al. Effect of thermal induced porosity on high-cycle fatigue and very high-cycle fatigue behaviors of hot-isostatic-pressed Ti-6Al-4V powder components. J Mater Sci Technol 2022;98:177–85.
[43] Soltani-Tehrani A, Isaac JP, Tippur HV, Silva DF, Shao S, Shamsaei N. Ti-6Al-4V powder reuse in laser powder bed fusion (L-PBF): The effect on porosity, microstructure, and mechanical behavior. Int J Fatigue 2023;167:107343.
[44] Soltani-Tehrani A, Habibnejad-Korayem M, Shao S, Haghshenas M, Shamsaei N. Ti-6Al-4V powder characteristics in laser powder bed fusion: The effect on tensile and fatigue behavior. Addit Manuf 2022;51:102584.
[45] Avateffazeli M, Shakil SI, Khan MF, Pirgazi H, Shamsaei N, Haghshenas M. The effect of heat treatment on fatigue response of laser powder bed fused Al-Cu-Mg-Ag-TiB2 (A20X) alloy. Mater Today Commun 2023;35:106009.
[46] Beretta S, Anderson C, Murakami Y. Extreme value models for the assessment of steels containing multiple types of inclusion. Acta Mater 2006;54(8):2277–89.
[47] Zhou S, Murakami Y, Beretta S, Fukushima Y. Experimental investigation on statistics of extremes for three-dimensional distribution of non-metallic inclusions. Mater Sci Technol 2002;18(12):1535–43.
[48] Kim J, Kim J, Pyo C. Comparison of mechanical properties of Ni-Al-Bronze alloy fabricated through wire arc additive manufacturing with Ni-Al-Bronze alloy fabricated through casting. Metals 2020;10(9):1164.
[49] Cai X, Yang M, Qiao Y, Wang Z, Zhou J, Xue F. Experimental investigation on wear resistance and corrosion behavior of nickel-aluminum bronze alloy fabricated by wire-arc additive manufacturing. J Mater Res Technol 2023;26:5801–15.
[50] Tian YZ, Zhao LJ, Chen S, Shibata A, Zhang ZF, Tsuji N. Significant contribution of stacking faults to the strain hardening behavior of Cu-15% Al alloy with different grain sizes. Sci Rep 2015;5(1):16707.
[51] Ma S, Fu L, Shan A. Enhancing strength-ductility of the aluminum bronze alloy by generating high-density ultrafine annealing twins. Mater Charact 2021;177: 111057.
[52] Zhang S, Wu L, Gu T, Shi Y, Tian X, Li H, et al. Effect of microstructure on the mechanical properties of ultrafine-grained Cu-Al-Ni alloys processed by deformation and annealing. J Alloy Compd 2022;923:166413.
[53] Zhang LM, Ma AL, Yu H, Umoh AJ, Zheng YG. Correlation of microstructure with cavitation erosion behaviour of a nickel-aluminum bronze in simulated seawater. Tribol Int 2019;136:250–8.
[54] Cai X, Wang Z, Dong L, Yang M, Zhou J, Xue F. Advanced mechanical properties of nickel-aluminum bronze/steel composite structure prepared by wire-arc additive manufacturing. Mater Des 2022;221:110969.
[55] Haghshenas M, Klassen RJ. Mechanical characterization of flow formed FCC alloys. Mater Sci Eng A 2015;641:249–55.
[56] Yadollahi A, Shamsaei N. Additive manufacturing of fatigue resistant materials: Challenges and opportunities. Int J Fatigue 2017;98:14–31.

[57] Shamsaei N, Yadollahi A, Bian L, Thompson SM. An overview of Direct Laser Deposition for additive manufacturing. Part II: Mechanical behavior, process parameter optimization and control. Add Manuf 2015;8:12–35.
[58] Yadollahi A, Shamsaei N, Thompson SM, Elwany A, Bian L. Effects of building orientation and heat treatment on fatigue behavior of selective laser melted 17–4 PH stainless steel. Int J Fatigue 2017;94:218–35.
[59] Shakerin S, Sanjari M, Amirkhiz BS, Mohammadi M. Interface engineering of additively manufactured maraging steel-H13 bimetallic structures. Mater Charact 2020;170:110728.
[60] Wei Z, Yuan M, Shen X, Han F, Yao Y, Xin L, et al. EBSD investigation on the interface microstructure evolution of Ti-Al3Ti laminated composites during the preparation process. Mater Charact 2020;165:110374.